ORIGINAL

COMPLETED

NASA Technical Paper 1789

Wind-Tunnel Measurements and Comparison With Flight of the Boundary Layer and Heat Transfer on a Hollow Cylinder at Mach 3

Robert L. Stallings, Jr., and Milton Lamb

DECEMBER 1980

NASA

NASA Technical Paper 1789

Wind-Tunnel Measurements and Comparison With Flight of the Boundary Layer and Heat Transfer on a Hollow Cylinder at Mach 3

Robert L. Stallings, Jr., and Milton Lamb
Langley Research Center
Hampton, Virginia

National Aeronautics
and Space Administration

**Scientific and Technical
Information Branch**

1980

SUMMARY

Wind-tunnel tests have been conducted to obtain boundary-layer and heat-transfer measurements on a hollow cylinder 304.22 cm in length and 43.70 cm in diameter for comparison with similar measurements that previously were obtained in flight with the same cylinder attached to the YF-12 airplane. The wind-tunnel tests were conducted both with and without boundary-layer trips at Mach 3 and nominal free-stream Reynolds numbers per meter ranging from 3.3×10^6 to 6.6×10^6. Instrumentation consisted of pressure orifices, thermocouples, a boundary-layer pitot pressure rake, and a floating element skin-friction balance. Measurements from both wind tunnel and flight are compared with existing engineering prediction methods.

Both wind-tunnel and flight heat-transfer measurements and skin-friction balance measurements using a virtual origin approximation from NASA TN D-7507 were in good agreement with the prediction methods of Sommer and Short and Spalding and Chi combined with the incompressible Karman-Schoenherr equation. A wind-tunnel measured Reynolds analogy factor of 1.125 was in good agreement with a flight measured value of 1.11. Good correlation of wind-tunnel and flight velocity profile measurements in the form of incompressible law-of-the-wall profiles were obtained using a wall reference temperature method. At equilibrium wall temperature conditions, boundary-layer transition Reynolds numbers from flight measurements for both the beginning and end of transition were generally greater than the wind-tunnel measured values.

INTRODUCTION

Several studies have been conducted within the National Aeronautics and Space Administration (NASA) to evaluate and develop engineering methods for predicting boundary-layer skin friction, heat transfer, and transition location for flight vehicles in supersonic and hypersonic flight (e.g., refs. 1, 2, 3, and 4). In general, the approach used in these studies is basically the same, i.e., to assemble a body of experimental data, reduce the data to a form that will facilitate comparison with theory or general correlations, and then determine the theories or correlations that best predict the results. Most of the experimental data used in these evaluations have been obtained in wind tunnels. Although flight data are desirable, only a limited amount exist in the literature (e.g., refs. 4, 5, and 6), and such data generally cannot be obtained under as well-controlled test conditions as are possible in wind tunnels. The NASA YF-12 research airplane program presented an opportunity to obtain flight measurements at Mach 3 cruise conditions in a controlled environment comparable to that available in wind tunnels. Therefore, a hollow cylinder 304.22 cm in length and 43.70 cm in diameter was fabricated, instrumented, and tested beneath the airplane fuselage as well as in the Langley Unitary Plan Wind Tunnel (UPWT). Instrumentation consisted of thermocouples, pressure orifices,

boundary-layer rake, and a floating element skin-friction balance. Flight measurements obtained at Mach 3 for cold wall and near equilibrium wall conditions have been published in reference 7.

This paper presents results obtained from testing the same instrumented cylinder in the Langley Unitary Plan Wind Tunnel at Mach 3 and nominal free-stream Reynolds numbers per meter ranging from 3.3×10^6 to 6.6×10^6. Measurements were obtained both with and without boundary-layer trips. The wind-tunnel results are compared with flight results and with several engineering prediction techniques also.

SYMBOLS

b	skin thickness
c	specific heat of model skin
c_p	specific heat of air at constant pressure
C_f	local skin-friction coefficient
C_F	average skin-friction coefficient
$F_c, F_{R\theta}, F_{Rx}$	functions defined by equations (20), (21), and (22), respectively
h	heat-transfer coefficient
M	Mach number
n	velocity profile power exponent defined by equation (38)
N_{Pr}	Prandtl number
N_{St}	Stanton number
p	static pressure
p_t	stagnation pressure
p'	pitot pressure
R	free-stream Reynolds number per meter
R_x	Reynolds number based on x_{eff} defined by equation (35)
$R_{x,b}$	Reynolds number based on x at beginning of transition (see fig. 3)
$R_{x,t}$	Reynolds number based on x at end of transition (see fig. 3)
R_θ	Reynolds number based on momentum thickness

s	Reynolds analogy factor, $2N_{St}/C_f$
t	time
T	static temperature
T_{aw}	adiabatic wall temperature
T_t	stagnation temperature
T_E	equilibrium wall temperature
u	velocity
u_τ	friction velocity, $\sqrt{\tau_w/\rho}$
x	distance downstream from leading edge of cylinder
x_{eff}	distance from virtual origin defined by equation (35)
x_t	value of x at transition location defined as peak temperature measurement or peak heat-transfer measurement
y	distance normal to cylinder
δ	boundary-layer thickness
δ_p	boundary-layer thickness determined from pitot pressure profile
δ^*	boundary-layer displacement thickness
η	recovery factor (see eq. (7))
θ	boundary-layer momentum thickness
μ	dynamic viscosity
ν	kinematic viscosity
ρ	air density
ρ_s	density of model skin
τ_w	wall shearing stress
ϕ	angular location of instrumentation (see fig. 1)

Subscripts:

e	conditions at outer edge of boundary layer in vicinity of boundary layer rake

w	wall conditions
w_{avg}	average wall conditions
ref	reference conditions
0, 1,...,n	time sequence
∞	free-stream conditions

A bar (-) over a symbol indicates incompressible value.

APPARATUS AND TEST CONDITIONS

This investigation was conducted in the high Mach number test section of the Langley Unitary Plan Wind Tunnel described in reference 8. It is a variable-pressure, continuous-flow tunnel with an asymmetrical sliding block nozzle that permits a continuous variation in the test-section Mach number from 2.30 to 4.65. For the present investigation, tests were conducted at a Mach number of 3.0 and nominal free-stream Reynolds numbers per meter of 3.3×10^6, 4.9×10^6, and 6.6×10^6. Test conditions for the heat-transfer tests are listed in table I; test conditions for the equilibrium wall temperature tests can be found in table II.

MODEL AND INSTRUMENTATION

The cylinder, as shown in figure 1, had an overall length of 304.22 cm and an outside diameter of 43.70 cm. Most of the pylon that was used to attach the cylinder to the airplane was removed for the wind-tunnel tests. A sting assembly was bolted to the remaining pylon stub such that the cylinder could be supported by the tunnel model support system. The cylinder was constructed with a thin outer skin to facilitate heat-transfer measurements. The outer skin had a nominal thickness of 0.13 cm. The main load-carrying structure of the cylinder consisted of a tube having a wall thickness of 0.64 cm and an inside diameter of 39.36 cm. The inside diameter of this tube formed the internal surface of the cylinder assembly. An air gap of 1.40 cm was maintained between the tube and outer skin to minimize internal conduction losses.

For the tunnel tests, the cylinder was instrumented with 123 thermocouples, 34 static pressure orifices, a skin-friction balance, and a pitot pressure rake. The thermocouples were 30-gage chromel alumel wires spot-welded to the inside surface of the skin. The pressure orifices consisted of tubing having an inside diameter of 0.32 cm and were installed flush with the external skin surface. Local shearing forces were measured by a floating-element skin-friction balance mounted so that the sensing element was flush with the external skin. It was located on the $\phi = 0^o$ ray 260.40 cm downstream from the cylinder leading edge. The balance was a self-nulling type instrument whose output voltage was directly proportional to the skin-friction force on the sensing element. The balance was commercially developed and is described in detail in reference 9. The pitot pressure rake (fig. 1(b)) was also located on the $\phi = 0^o$ ray with

the ends of the pitot probes located 274.12 cm downstream from the cylinder leading edge. The conical probe located outboard of the pitot probes was used to determine local flow angularity for the flight tests and was not used in the wind-tunnel tests. Measurements from the stagnation temperature rake were not obtained in the wind-tunnel tests because of damage to a connector cable internal to the cylinder after the flight tests.

DATA REDUCTION

For all data reduction the gas was assumed to be ideal and the viscosity was determined by the Keyes formula (ref. 10) as follows:

$$\mu = \frac{(1.49 \times 10^{-6})T^{1/2}}{1 + (122.2/T)10^{-5/T}} \tag{1}$$

where T is in K and μ is in Pa-s.

Boundary-Layer Rake

The wall temperature used in the calculation of the rake data was the average of the measured wall temperatures on the cylinder ray ahead of the rake. The following parameters were calculated from the rake pressure measurements combined with a measured static pressure located 7.62 cm ahead of the rake. The static pressure was assumed to remain constant across the boundary layer. Velocities were calculated by combining the equation

$$\frac{u}{u_e} = \frac{M}{M_e}\sqrt{\frac{1 + 0.2M_e^2}{1 + 0.2M^2}}\sqrt{\frac{T_t}{T_{t,e}}} \tag{2}$$

with the quadratic total temperature distribution from ref. 11

$$\frac{T_t}{T_{t,e}} = \left(1 - \frac{T_{aw}}{T_{t,e}}\right)\left(\frac{u}{u_e}\right)^2 + \left(\frac{T_{aw}}{T_{t,e}} - \frac{T_w}{T_{t,e}}\right)\frac{u}{u_e} + \frac{T_w}{T_{t,e}} \tag{3}$$

Equation (3) is in good agreement with the flight total temperature profiles (ref. 7) and also gives good agreement with wind-tunnel measured profiles for flat-plate type flows given in reference 12. The resulting equation is

$$\frac{u}{u_e} = \frac{\frac{T_w}{T_{t,e}} - \frac{T_{aw}}{T_{t,e}} - \sqrt{\left(\frac{T_{aw}}{T_{t,e}} + \frac{T_w}{T_{t,e}}\right)^2 - 4\,\frac{T_w}{T_{t,e}}(1 - k)}}{2\left(1 - \frac{T_{aw}}{T_{t,e}}\right) - 2k} \tag{4}$$

where

$$k = \left(\frac{M_e}{M}\right)^2\left(\frac{1 + 0.2M^2}{1 + 0.2M_e^2}\right) \tag{5}$$

and

$$\frac{T_{aw}}{T_{t,e}} = \frac{1 + 0.2\eta M_e^2}{1 + 0.2M_e^2} \tag{6}$$

For all rake calculations, the boundary layer was turbulent and it was assumed that

$$\eta = (N_{Pr})^{1/3} \tag{7}$$

Boundary-layer momentum thickness and displacement thickness were calculated from the equations

$$\theta = \int_0^{\delta} \frac{\rho u}{\rho_e u_e}\left(1 - \frac{u}{u_e}\right)\,dy \tag{8}$$

$$\delta^* = \int_0^{\delta} \left(1 - \frac{\rho u}{\rho_e u_e}\right)\,dy \tag{9}$$

The mixing length transformation of Van Driest and several reference temperature transformations were used to convert the measured velocity profiles to incompressible law-of-the-wall profiles. Equations for these transformations are given as equations (10) to (18). For the Van Driest method (ref. 13),

$$\frac{\bar{u}}{\bar{u}_\tau} = \frac{1}{A\sqrt{(C_f/2)(T_w/T_e)}}\left(\sin^{-1}\frac{2A^2(u/u_e) - B}{\sqrt{B^2 + 4A^2}} + \sin^{-1}\frac{B}{\sqrt{B^2 + 4A^2}}\right) \tag{10}$$

and

$$\frac{\bar{u}_\tau \bar{y}}{\bar{\nu}} = (u_e y/\nu_w)\sqrt{(C_f/2)(T_w/T_e)} \tag{11}$$

where

$$A = \sqrt{(T_e/T_w)(0.2M_e^2)} \tag{12}$$

$$B = (T_e/T_w) + A^2 - 1 \tag{13}$$

and C_f is measured with a floating element skin-friction balance. For the reference temperature transformations,

$$\frac{\bar{u}}{\bar{u}_\tau} = \frac{u/u_e}{\sqrt{(C_f/2)(T_{ref}/T_e)}} \tag{14}$$

and

$$\frac{\bar{u}_\tau \bar{y}}{\bar{\nu}} = (u_e y/\nu_{ref})\sqrt{(C_f/2)(T_{ref}/T_e)} \tag{15}$$

where the following three methods were used to define T_{ref}:

(1) Wall reference temperature method

$$T_{ref} = T_w \tag{16}$$

(2) Sommer and Short T-Prime method (ref. 14)

$$\frac{T_{ref}}{T_e} = 1 + 0.035M_e^2 + 0.45\left(\frac{T_w}{T_e} - 1\right) \tag{17}$$

(3) Eckert reference wall temperature (ref. 15)

$$\frac{T_{ref}}{T_e} = 0.5\left(\frac{T_w}{T_e} + 1\right) + 0.22\left(\frac{T_{aw}}{T_e} - 1\right) \tag{18}$$

Skin-Friction Balance Measurements

Measured shearing forces from the floating element skin-friction balance were converted to skin-friction coefficients using the equation

$$C_f = \frac{\tau_w}{1/2\ \rho_\infty u_\infty^2} \tag{19}$$

The measured values of C_f and Reynolds number were converted to incompressible values using the following equations from reference 2:

$$\bar{C}_f = F_C C_f \tag{20}$$

$$\bar{R}_{\bar{\theta}} = F_{R\theta} R_\theta \tag{21}$$

$$\bar{R}_{\bar{x}} = F_{Rx} R_x \tag{22}$$

$$F_{Rx} = \frac{F_{R\theta}}{F_C} \tag{23}$$

The transformation factors F_C and $F_{R\theta}$ were determined from four different methods as follows. For the Spalding and Chi method (ref. 16),

$$F_C = \frac{(T_{aw}/T_e) - 1}{(\sin^{-1}\alpha + \sin^{-1}\beta)^2} \tag{24}$$

where

$$\alpha = \frac{\frac{T_{aw}}{T_e} + \frac{T_w}{T_e} - 2}{\left[\left(\frac{T_{aw}}{T_e} + \frac{T_w}{T_e}\right)^2 - 4\frac{T_w}{T_e}\right]^{1/2}} \tag{25}$$

$$\beta = \frac{\frac{T_{aw}}{T_e} - \frac{T_w}{T_e}}{\left[\left(\frac{T_{aw}}{T_e} + \frac{T_w}{T_e}\right)^2 - 4\frac{T_w}{T_e}\right]^{1/2}} \tag{26}$$

and

$$F_{R\theta} = \left(\frac{T_{aw}}{T_e}\right)^{0.772}\left(\frac{T_w}{T_e}\right)^{-1.474} \tag{27}$$

For the Van Driest method (Van Driest II, ref. 17), F_C is determined from equations (24), (25), and (26) and

$$F_{R\theta} = \frac{\mu_e}{\mu_w} \tag{28}$$

For the two reference temperature methods used,

$$F_C = \frac{T_{ref}}{T_e} \tag{29}$$

and

$$F_{R\theta} = \frac{\mu_e}{\mu_{ref}} \tag{30}$$

where equations (29) and (30) were evaluated using the reference temperature method of Sommer and Short, equation (17), and the reference temperature method of Eckert, equation (18).

Heat-Transfer Measurements

The heat-transfer measurements were obtained from transient skin-temperature measurements resulting from a stepwise increase in stagnation temperature. This technique is described in detail in ref. 18.

The heat balance equation reduces to

$$h = \frac{\rho_s bc \dfrac{dT_w}{dt}}{T_E - T_w} \tag{31}$$

when it is assumed that there is negligible lateral heat flow, constant temperature through the model skin, negligible heat flow to the model interior, and no heat losses due to radiation.

Equation (31) can be integrated and written in the following form for complete machine calculation:

$$h = \frac{\rho_s bc (T_{w,n} - T_{w,0})}{\dfrac{T_E}{T_t}\displaystyle\int_0^t T_t \, dt - \int_0^t T_w \, dt} \tag{32}$$

The integrals of equation (32) were evaluated using the trapezoidal rule. Prior to the increase in stagnation temperature, T_E is measured, and the ratio T_E/T_t is assumed to be independent of T_t based on previous measurements. The heat-transfer coefficients were converted to Stanton numbers using the equation

$$N_{St} = \frac{h}{\rho_\infty u_\infty c_p} \tag{33}$$

Skin-friction coefficients were determined from Stanton numbers through Reynolds analogy using the equation

$$C_f = \frac{2N_{St}}{s} \tag{34}$$

where the value of the Reynolds analogy factor s was determined experimentally. These compressible skin-friction coefficients were then transformed to incompressible values using equations (20) to (30) and using local measured wall temperatures.

RESULTS AND DISCUSSION

The skin-friction balance and boundary-layer rake measurements were obtained with the model at equilibrium wall conditions and a nominal stagnation temperature of 339 K; the measurements are tabulated in table II. The heat-transfer measurements were obtained under transient cold-wall conditions and a stagnation temperature of approximately 394 K; these results are tabulated in table III.

Surface Static Pressure

The cylinder was instrumented with static pressure orifices to determine local flow conditions as well as to establish the two dimensionality of the flow field and to determine if any extraneous shock waves intersected the cylinder. The orifices were located along the $\phi = 0^\circ$ cylinder ray and at several circumferential locations as shown in figure 1. Typical pressure distributions measured at equilibrium wall conditions, nondimensionalized by free-stream static pressure both with and without transition grit, are shown in figure 2. The free-stream static pressure was determined from measured free-stream stagnation pressure and a free-stream Mach number from previous calibrations. Although there is some small scatter in the data, it is generally less than the instrumentation accuracy. These results indicate that the cylinder was properly aligned with the flow and that there were no significant effects of reflected shock waves.

Boundary-Layer Transition

For the equilibrium temperature tests, the beginning of boundary-layer transition was assumed to be located at the point where the wall temperature

initially began increasing due to transition and the end of transition was assumed to be located at the peak measured wall temperatures as illustrated in figure 3. For the heat-transfer tests discussed subsequently, similar procedures were used for defining the location of transition using heat-transfer coefficients rather than temperatures. This technique is consistent with other methods of locating transition as discussed in reference 19. The transition locations for the equilibrium temperature tests are given in table II. It should be noted that the value of x_t given in table II(f) was not measured but was approximated, based on comparisons with the heat-transfer data to be discussed subsequently.

Shown in figure 4 are comparisons of transitional Reynolds numbers measured in the wind tunnel with those measured in flight. The results shown in figures 4(a) and 4(b) are for the case of no boundary-layer trip and for the beginning and end of transition, respectively. The wind-tunnel data for this no-trip case show an increase in transition Reynolds number at both the beginning and end of transition with a decrease in T_w/T_t. This trend is to be expected since, for this range of T_w/T_t, an increase in the amount of cooling generally results in an increase in boundary-layer stability. The flight transitional Reynolds numbers for $T_w/T_t = 0.85$ are much larger than the tunnel values. The smaller tunnel values are probably a result of noise generated by the turbulent boundary layer on the nozzle side wall increasing the disturbance level within the model flow field and, hence, moving the location of transition forward. This phenomenon is a characteristic of most supersonic wind tunnels and is well documented in the literature (e.g., ref. 4). The flight transitional Reynolds number shown in figure 4(b) for $0.62 \leq T_w/T_t \leq 0.67$ is much lower than the flight results at $T_w/T_t = 0.85$ or even the tunnel results. As discussed in reference 7, this reduced transitional Reynolds number is believed to result from some unknown phenomenon causing the boundary layer to artificially trip. This low transition Reynolds number for flight is in fair agreement with the tunnel transitional Reynolds numbers obtained downstream of a boundary-layer trip consisting of No. 35 transition grit, as shown in figure 4(c).

Virtual Origin Location

For all boundary-layer calculations and correlations requiring an effective length of turbulent boundary-layer run, best results for the present tests were obtained using the following empirical equation from reference 2:

$$x_{eff} = x - 0.825x_t \tag{35}$$

where x is the longitudinal surface distance relative to the leading edge and x_t is the value of x at the location of the end of transition, as previously discussed. Equation (35) was used to determine the virtual origin for both wind-tunnel data and flight data that are presented in this report.

Boundary-Layer Thickness and Momentum Thickness

Boundary-layer thicknesses were determined from the rake impact pressure measurements using the same technique that was used for the flight tests (ref. 7) and that is described in reference 11. This method, as shown in figure 5, consists of extrapolating the linear variation of p'/p_e with y in the outer region of the boundary layer to the local measured free-stream value of p'/p_e. For all rake calculations, local static pressures were assumed to correspond to the values measured at the orifice located 7.62 cm ahead of the rake.

Shown in figure 6 are momentum thicknesses calculated from the rake data using equation (8). Also shown for comparison with the experimental data are several theoretical calculations. The theoretical momentum thicknesses were determined using the relationship

$$\frac{\theta}{x_{eff}} = \frac{C_F}{2} \tag{36}$$

where the average skin-friction coefficient C_F was determined by the different theories. The Sommer and Short (ref. 14), Spalding and Chi (ref. 16), and Eckert (ref. 15) theoretical values are based on an incompressible $\bar{C}_F$ from the Karman-Schoenherr equation

$$\frac{0.242}{\sqrt{\bar{C}_F}} = \log_{10} (\bar{R}_x \bar{C}_F) \tag{37}$$

The magnitude of the experimental data, as shown in figure 6, ranges between the calculated values from the reference temperature methods of Sommer and Short and Eckert. The theories of Shapiro (ref. 22) and Spalding and Chi generally overpredict the experimental data for the test range of Reynolds numbers.

Velocity Profiles

The measured nondimensional velocity profiles are compared with a power law relationship of the form

$$\frac{u}{u_e} = \left(\frac{y}{\delta_p}\right)^{1/n} \tag{38}$$

in figure 7(a) without transition grit and in figure 7(b) with No. 35 transition grit. The data for the three Reynolds numbers in each figure collapse

into a narrow band and are generally in good agreement with equation (53) when n has a value of 7. The insensitivity of n to R_θ is consistent with the results presented in figure 13 of reference 20 for the same range of R_θ.

Velocity profiles measured both in the wind tunnel and in flight were transformed to incompressible law-of-the-wall profiles using the four methods described in the Data Reduction section. These transformations are all based on measured skin-friction coefficients. The profiles are shown in figure 8 and are compared with the Coles incompressible curve (ref. 21). The best correlation of flight and wind-tunnel data was obtained using the reference wall temperature method with the band of data falling below Coles incompressible curve. The other three methods resulted in less satisfactory correlation of the flight and wind-tunnel data with magnitudes that were generally greater than the Coles curve. Although not shown, data obtained with the No. 35 transition grit resulted in the same trends.

Skin-Friction Balance Data

Skin-friction balance measurements obtained in the wind tunnel for the three test Reynolds numbers with and without boundary-layer trips are compared with flight data in figure 9. The two flight data points represent two different wall temperatures at almost the same unit Reynolds number. The data have been reduced to incompressible skin-friction coefficients and incompressible effective length Reynolds numbers using the four transformation methods described in the Data Reduction section. For these comparisons, Reynolds numbers for the flight data are also based on an effective length determined from equation (37) where the location of boundary-layer transition was determined from the temperature and heat-transfer distributions of reference 7. The Karman-Schoenherr incompressible curve is shown in figure 9 for comparison with the measured data. The results show that best correlation of flight and wind-tunnel data is obtained using the Eckert reference temperature method and the Sommer and Short method and that best agreement with the Karman-Schoenherr incompressible curve is obtained using the Sommer and Short method. The other three methods give results that generally are within ±5 percent of the Karman-Schoenherr incompressible curve. It was concluded in reference 7 that the Van Driest transformation gave best agreement between flight data and incompressible theory. This agreement is also shown in figure 9 for the present analysis; however, the Van Driest transformation does not give as good a correlation between flight and tunnel data as was obtained with the reference temperature methods.

Heat-Transfer Measurements

The measured wind-tunnel heat-transfer distributions for the three test Reynolds numbers both with and without boundary-layer trips are shown in figure 10. Results are presented for the primary instrumentation ray ($\phi = 0^\circ$) and for the diametrically opposite ray ($\phi = 180^\circ$). With the exception in some cases of a slight difference in the location of boundary-layer transition (assumed to be located at peak heating) and its effect on local heating rates, the heating rates on each side of the cylinder are approximately equal. The circumferential heat-transfer distributions were essentially constant with ϕ

and therefore are not shown. The locations of boundary-layer transition as determined from the heating rates at $\phi = 0^{\circ}$ are listed in table I. The location of transition for $R = 6.69 \times 10^6$ with a boundary-layer trip (fig. 10(b)) could not be determined from the heat-transfer measurements since peak heating occurred ahead of the first instrumentation location. The value of x_t used in equation (35) for all calculations at these conditions was determined as the value that best correlated the turbulent measurements for this run with the turbulent measurements of the other five runs in the form of Stanton numbers versus effective Reynolds numbers.

In order to compare the wind-tunnel and flight heat-transfer data and to compare both sets of data with existing prediction methods, the heat-transfer measurements were converted to skin-friction coefficients using a measured Reynolds analogy factor of 1.125. This value of the Reynolds analogy factor was determined from the heat-transfer and skin-friction balance measurements and is in good agreement with the flight measured value of 1.11 (ref. 7). The compressible skin-friction coefficients were then transformed to incompressible values using the four methods discussed in the Data Reduction section. These results are shown in figure 11(a) for the no-trip case and in figure 11(b) for the trip case. The circle symbols are wind-tunnel data for three test Reynolds numbers and the square symbols are flight data from ref. 7. For these comparisons, the flight data were transformed to incompressible form using the same equations that were used for the wind-tunnel data. It should be noted that only the turbulent heat-transfer measurements were used to derive the results shown in figure 11 and that for both the wind-tunnel and flight data, all Reynolds numbers are based on an effective distance determined from equation (35). In general, the comparisons show that all four methods satisfactorily correlate the data and that the Spalding and Chi and Sommer and Short reference temperature methods result in the best agreement with the Karman-Schoenherr incompressible curve. Results from the Van Driest method are generally below the Karman-Schoenherr incompressible curve; whereas, results from the Eckert reference temperature methods are generally greater. These same trends were shown by the skin-friction balance data previously discussed and presented in figure 9.

SUMMARY OF RESULTS

Wind-tunnel tests have been conducted to obtain boundary-layer and heat-transfer measurements on a hollow cylinder 304.22 cm in length and 43.70 cm in diameter for comparison with similar measurements that previously were obtained in flight with the same cylinder attached to the YF-12 airplane. The wind-tunnel tests were conducted both with and without boundary-layer trips at Mach 3 and nominal free-stream Reynolds numbers per meter ranging from 3.3×10^6 to 6.6×10^6. Instrumentation consisted of pressure orifices, thermocouples, a boundary-layer pitot pressure rake, and a floating element skin-friction balance. Measurements from both wind tunnel and flight are compared with existing engineering prediction methods. The results are summarized as follows:

1. Good correlation of wind-tunnel and flight velocity profile measurements in the form of incompressible law-of-the-wall profiles were obtained using a wall reference temperature method.

2. Best agreement between wind-tunnel and flight skin-friction balance measurements and predicted results were obtained using the Sommer and Short Reference Tempeature Method.

3. A Reynolds analogy factor of 1.125 was determined from the wind-tunnel skin-friction balance and heat-transfer measurements and is in good agreement with the flight measured value of 1.11.

4. Both wind-tunnel and flight heat-transfer measurements using a virtual origin approximation from NASA TN D-7507 were in good agreement with the prediction methods of Spalding and Chi and Sommer and Short.

5. At equilibrium wall temperature conditions, boundary-layer transition Reynolds numbers from flight measurements for both the beginning and end of transition were generally greater than the wind-tunnel measured values.

Langley Research Center
National Aeronautics and Space Administration
Hampton, VA 23665
November 26, 1980

REFERENCES

1. Peterson, John B., Jr.: A Comparison of Experimental and Theoretical Results for the Compressible Turbulent-Boundary-Layer Skin Friction With Zero Pressure Gradient. NASA TN D-1795, 1963.

2. Cary, Aubrey M., Jr.; and Bertram, Mitchel H.: Engineering Prediction of Turbulent Skin Friction and Heat Transfer in High-Speed Flow. NASA TN D-7507, 1974.

3. Hopkins, Edward J.; Rubesin, Morris W.; Inouye, Mamoru; Keener, Earl R.; Mateer, George C.; and Polek, Thomas E.: Summary and Correlation of Skin-Friction and Heat-Transfer Data for a Hypersonic Turbulent Boundary Layer on Simple Shapes. NASA TN D-5089, 1969.

4. Dougherty, N. S., Jr.; and Fisher, D. F.: Boundary-Layer Transition on a 10-Deg Cone: Wind Tunnel/Flight Correlation. AIAA-80-0154, Jan. 1980.

5. Zoby, Ernest V.; and Rumsey, Charles B.: Analysis of Free-Flight Laminar, Transitional, and Turbulent Heat-Transfer Results at Free-Stream Mach Numbers Near 20 (Reentry F). NASA TM X-2335, 1971.

6. Quinn, Robert D.; and Olinger, Frank V. (appendix A by James C. Dunavant and Robert L. Stallings, Jr.): Heat-Transfer Measurements Obtained on the X-15 Airplane Including Correlations With Wind-Tunnel Results. NASA TM X-1705, 1969.

7. Quinn, Robert D.; and Gong, Leslie: In-Flight Compressible Turbulent Boundary Layer Measurements on a Hollow Cylinder at a Mach Number of 3.0. YF-12 Experiments Symposium - Volume 1, NASA-CP-2054, 1978, pp. 259-286.

8. Manual for Users of the Unitary Plan Wind Tunnel Facilities of the National Advisory Committee for Aeronautics. NASA, 1956.

9. Paros, Jerome M.: Application of the Force-Balance Principle to Pressure and Skin Friction Sensors. 16th Annual Technical Meeting Proceedings, Inst. Environ. Sci., 1970, pp. 363-368.

10. Keyes, F. G.: A Summary of Viscosity and Heat-Conduction Data for He, A, H_2, O_2, N_2, CO, CO_2, H_2O, and Air. Trans. ASME, vol. 73, no. 5, July 1951, pp. 589-596.

11. Samuels, Richard D.; Peterson, John B., Jr.; and Adcock, Jerry B.: Experimental Investigation of the Turbulent Boundary Layer at a Mach Number of 6 With Heat Transfer at High Reynolds Numbers. NASA TN D-3858, 1967.

12. Bushnell, Dennis M.; Johnson, Charles B.; Harvey, William D.; and Feller, William V.: Comparison of Prediction Methods and Studies of Relaxation in Hypersonic Turbulent Nozzle-Wall Boundary Layers. NASA TN D-5433, 1969.

13. Van Driest, E. R.: Turbulent Boundary Layer in Compressible Fluids. J. Aeronaut. Sci., vol. 18, no. 3., Mar. 1951, pp. 145-160, 216.

14. Sommer, Simon C.; and Short, Barbara J.: Free-Flight Measurements of Turbulent-Boundary-Layer Skin Friction in the Presence of Severe Aerodynamic Heating at Mach Numbers From 2.8 to 7.0. NACA TN 3391, 1955.

15. Eckert, E. R. G.: Engineering Relations for Friction and Heat Transfer to Surfaces in High Velocity Flow. J. Aeronaut. Sci., vol. 22, no. 8, Aug. 1955, pp. 585-587.

16. Spalding, D. B.; and Chi, S. W.: The Drag of a Compressible Turbulent Boundary Layer on a Smooth Flat Plate With and Without Heat Transfer. J. Fluid Mech., vol. 18, pt. 1, Jan. 1964, pp. 117-143.

17. Van Driest, E. R.: The Problem of Aerodynamic Heating. Aeronaut. Eng. Rev., vol. 15, no. 10, Oct. 1956, pp. 26-41.

18. Burbank, Paige B.; and Hodge, B. Leon: Distribution of Heat Transfer on a 10° Cone at Angles of Attack From 0° to 15° for Mach Numbers of 2.49 to 4.65 and a Solution to the Heat-Transfer Equation that Permits Complete Machine Calculations. NASA MEMO 6-4-59L, 1959.

19. Potter, J. Leith; and Whitfield, Jack D.: Effects of Unit Reynolds Number, Nose Bluntness, and Roughness on Boundary Layer Transition. AEDC-TR-60-5, U.S. Air Force, Mar. 1960.

20. Keener, Earl R.; and Hopkins, Edward J.: Turbulent Boundary-Layer Velocity Profiles on a Nonadiabatic Flat Plate at Mach Number 6.5. NASA TN D-6907, 1972.

21. Coles, Donald: Measurements in the Boundary Layer on a Smooth Flat Plate in Supersonic Flow - I. The Problem of the Turbulent Boundary Layer. Rep. 20-69 (Contract No. DA-04-495-Ord 18), Jet Propulsion Lab., California Inst. Technol., June 1, 1953.

22. Shapiro, Ascher H.: The Dynamics and Thermodynamics of Compressible Fluid Flow. Vol. II. Ronald Press Co., c.1954, p. 1110.

TABLE I.- HEAT-TRANSFER TEST CONDITIONS

Transition grit	R	$T_{w,avg}/T_t$	T_t, K	$x_{t,\phi=0}$, cm
No. 35	3.46×10^6	0.811	391	63.5
No. 35	5.12	.801	392	25.4
None	6.69	.798	393	11.4
None	3.40	.809	394	99.1
None	5.11	.794	396	73.7
None	6.67	.795	397	63.5

TABLE II.- BOUNDARY-LAYER SURVEYS

(a) Without grit $C_f = 0.00159$

$R = 3.29 \times 10^6$ $\delta = 3.32$ cm

$M_e = 3.008$ $\delta^* = 1.11$ cm

$p_e = 1.46$ kPa $\theta = 0.209$ cm

$T_{w,avg} = 312$ K $x_t = 71.1$ cm

$T_t = 339$ K $p_{t,\infty} = 53.2$ kPa

y, cm	M/M_e	u/u_e
0.312	0.5329	0.7128
.506	.5957	.7674
.693	.6340	.7978
.887	.6672	.8224
1.057	.6935	.8409
1.435	.7513	.8784
2.098	.8481	.9326
2.703	.9302	.9714
3.312	.9761	.9906
3.934	.9990	.9996
4.547	1.0000	1.0000

(b) Without grit $C_f = 0.00148$

$R = 4.92 \times 10^6$ $\delta = 3.20$ cm

$M_e = 2.966$ $\delta^* = 1.06$ cm

$p_e = 2.26$ kPa $\theta = 0.203$ cm

$T_{w,avg} = 315$ K $x_t = 58.4$ cm

$T_t = 339$ K $p_{t,\infty} = 79.7$ kPa

y, cm	M/M_e	u/u_e
0.312	0.5465	0.7230
.506	.6079	.7753
.693	.6423	.8022
.887	.6760	.8270
1.057	.7023	.8453
1.435	.7600	.8823
2.098	.8597	.9377
2.703	.9410	.9758
3.312	.9831	.9933
3.934	1.0000	1.0000

TABLE II.- Continued

(c) Without grit $C_f = 0.00144$

$R = 6.57 \times 10^6$ $\delta = 3.12$ cm

$M_e = 2.944$ $\delta^* = 1.02$ cm

$p_e = 3.07$ kPa $\theta = 0.196$ cm

$T_{w,avg} = 316$ K $x_t = 43.2$ cm

$T_t = 339$ K $p_{t,\infty} = 106.3$ kPa

y, cm	M/M_e	u/u_e
0.312	0.5605	0.7338
.506	.6186	.7824
.693	.6546	.8101
.887	.6855	.8325
1.057	.7113	.8498
1.435	.7721	.8888
2.098	.8689	.9418
2.703	.9484	.9788
3.312	.9868	.9947
3.934	1.0000	1.0000

(d) No. 35 grit $C_f = 0.00159$

$R = 3.27 \times 10^6$ $\delta = 3.25$ cm

$M_e = 3.033$ $\delta^* = 1.11$ cm

$p_e = 1.44$ kPa $\theta = 0.208$ cm

$T_{w,avg} = 311$ K $x_t = 73.7$ cm

$T_t = 339$ K $p_{t,\infty} = 53.0$ kPa

y, cm	M/M_e	u/u_e
0.312	0.5351	0.7160
.506	.5945	.7675
.693	.6334	.7983
.887	.6677	.8237
1.057	.6924	.8410
1.435	.7517	.8793
2.098	.8487	.9333
2.703	.9291	.9711
3.312	.9759	.9906
3.934	.9993	.9998
4.547	1.0000	1.0000

TABLE II.- Concluded

(e) No. 35 grit $C_f = 0.00145$

$R = 4.93 \times 10^6$ $\delta = 3.38$ cm

$M_e = 2.975$ $\delta^* = 1.14$ cm

$p_e = 2.25$ kPa $\theta = 0.219$ cm

$T_{w,avg} = 313$ K $x_t = 22.9$ cm

$T_t = 339$ K $p_{t,\infty} = 79.7$ kPa

y, cm	M/M_e	u/u_e
0.312	0.5405	0.7176
.506	.6003	.7693
.693	.6343	.7962
.887	.6649	.8191
1.057	.6884	.8358
1.435	.7412	.8708
2.098	.8370	.9261
2.703	.9180	.9656
3.312	.9708	.9883
3.934	.9990	.9996
4.547	1.0000	1.0000

(f) No. 35 grit $C_f = 0.00140$

$R = 6.57 \times 10^6$ $\delta = 3.35$ cm

$M_e = 2.950$ $\delta^* = 1.11$ cm

$p_e = 3.05$ kPa $\theta = 0.214$ cm

$T_{w,avg} = 314$ K $x_t = 10.2$ cm

$T_t = 339$ K $p_{t,\infty} = 106.3$ kPa

y, cm	M/M_e	u/u_e
0.312	0.5563	0.7302
.506	.6119	.7772
.693	.6437	.8021
.887	.6732	.8239
1.057	.6980	.8413
1.435	.7532	.8774
2.098	.8454	.9299
2.703	.9207	.9665
3.312	.9739	.9895
3.934	.9993	.9997
4.547	1.0000	1.0000

TABLE III.- TABULATION OF HEAT-TRANSFER MEASUREMENTS

(a) No. 35 transition gr

ϕ, deg	x, cm	h, J/m^2-sec-K, for -			ϕ, deg	x, cm	h, J/m^2-sec-K, for -		
		R = 3.46 × 10^6	R = 5.12 × 10^6	R = 6.69 × 10^6			R = 3.46 × 10^6	R = 5.12 × 10^6	R = 6.69 × 10^6
0	15.24	14.84	26.60	96.35	0	147.32	32.55	44.26	56.43
	20.32	12.61	64.14	89.66		149.86	32.52	43.93	57.00
	22.86	11.63	74.86	86.19		152.40	34.43	46.81	60.27
	25.40	11.28	76.23	85.13		157.48	34.34	44.64	58.13
	27.94	10.97	72.43	82.67		162.56	36.14	47.46	58.95
	33.02	9.00	66.67	78.63		172.72	33.67	45.70	58.52
	43.18	14.49	60.15	73.29		177.80	31.28	43.45	58.17
	48.26	26.19	58.04	70.40		182.88	33.02	45.12	58.04
	50.80	33.09	57.53	71.70		187.96	31.64	43.16	57.73
	53.34	37.50	57.47	69.97		193.04	33.75	44.75	57.28
	55.88	44.42	56.87	69.34		203.20	32.37	44.07	56.70
	58.42	46.53	56.23	69.69		208.28	30.93	45.54	56.85
	60.96	47.56	55.59	69.13		213.36	30.67	42.98	56.91
	63.50	44.83	50.94	66.62		218.44	29.94	42.25	55.74
	66.04	47.30	54.44	68.04		223.52	30.70	43.40	56.27
	68.58	46.93	54.06	66.32		233.68	30.56	42.96	56.17
	71.12	45.07	53.67	66.58		238.76	31.68	44.03	56.25
	73.66	44.64	52.99	66.63		243.84	30.11	42.44	54.91
	78.74	41.62	51.80	62.79		248.92	31.19	43.46	55.55
	81.28	41.60	50.80	63.69		251.46	30.73	42.17	55.31
	83.82	41.25	51.16	65.03		254.00	29.97	41.16	55.52
	86.36	41.22	49.42	62.40		270.51	29.73	41.42	53.06
	88.90	40.86	51.88	63.69	180	17.78	14.88	76.63	90.45
	91.44	38.76	49.90	64.86		25.40	13.70	70.79	86.48
	93.98	38.73	49.92	63.81		33.02	16.37	65.81	80.82
	96.52	38.35	50.55	63.40		48.26	40.85	57.46	72.20
	99.06	38.62	48.50	63.12		55.88	47.76	57.59	71.86
	101.60	38.24	49.44	62.01		63.50	47.26	55.33	69.22
	104.14	38.16	49.71	62.31		71.12	44.60	53.93	67.50
	109.22	36.70	48.30	61.53		78.74	42.70	52.58	66.15
	111.76	37.46	48.35	61.30		86.36	41.85	52.15	65.76
	114.30	37.06	48.67	60.25		93.98	40.72	50.81	64.75
	116.84	37.10	48.37	61.65		101.60	40.51	49.28	62.94
	119.38	36.72	48.07	61.59		109.22	38.81	48.99	63.94
	121.92	37.79	49.40	62.71		116.84	38.36	49.25	62.87
	124.46	36.39	48.42	63.04		124.46	35.88	48.22	62.50
	127.00	36.00	48.02	61.63		132.08	36.23	48.24	62.50
	129.54	35.20	46.92	60.81		139.70	33.37	45.84	62.16
	132.08	34.47	46.83	59.39		147.32	33.69	46.81	60.70
	134.62	34.76	46.45	58.33		162.56	32.85	45.22	58.79
	139.70	32.88	44.64	57.49		175.26	33.19	46.26	59.84
	144.78	34.00	46.07	59.91					

TABLE III.- TABULATION OF HEAT-TRANSFER MEASUREMENTS

(b) Without transition grit

ϕ, deg	x, cm	h, J/m^2-sec-K, for -			ϕ, deg	x, cm	h, J/m^2-sec-K, for -		
		R = 3.40 × 10^6	R = 5.11 × 10^6	R = 6.67 × 10^6			R = 3.40 × 10^6	R = 5.11 × 10^6	R = 6.67 × 10^6
0	15.24	13.82	18.09	21.17	0	147.32	36.07	49.38	60.24
	20.32	11.14	14.61	17.64		149.86	34.42	50.31	61.48
	22.86	11.43	13.13	15.85		152.40	36.52	52.15	62.80
	25.40	11.10	13.09	14.65		157.48	34.39	46.45	59.37
	27.94	10.48	12.50	14.67		162.56	35.47	51.17	62.20
	33.02	8.34	11.87	14.46		172.72	35.39	47.88	61.11
	43.18	6.46	10.50	20.71		177.80	33.16	49.45	60.98
	48.26	7.41	12.93	30.52		182.88	35.46	48.54	61.14
	50.80	7.15	14.96	42.25		187.96	36.13	48.53	61.82
	53.34	7.48	16.32	48.76		193.04	35.47	48.55	61.69
	55.88	8.15	20.21	66.69		203.20	33.47	46.57	61.22
	58.42	8.23	23.76	77.09		208.28	30.52	47.10	59.82
	60.96	10.19	33.16	86.73		213.36	32.19	46.82	59.91
	63.50	10.93	36.19	89.15		218.44	31.18	44.52	58.09
	66.04	11.63	50.00	89.07		223.52	30.28	45.61	58.97
	68.58	12.99	56.12	87.19		233.68	32.74	46.37	57.82
	71.12	15.29	61.93	84.08		238.76	32.50	48.33	59.17
	73.66	17.91	68.29	84.77		243.84	30.37	44.59	56.88
	78.74	24.51	67.92	75.59		248.92	31.66	46.21	59.17
	81.28	29.82	66.17	76.98		251.46	31.26	44.84	57.38
	83.82	35.83	66.42	76.93		254.00	30.19	44.32	56.80
	86.36	39.55	63.76	76.89		270.51	29.64	42.42	53.96
	88.90	42.30	63.41	74.10	180	17.78	13.56	18.70	18.19
	91.44	44.13	61.78	75.20		25.40	10.86	14.64	17.52
	93.98	47.09	60.03	71.63		33.02	9.88	13.19	22.02
	96.52	46.42	59.67	71.69		48.26	8.75	26.63	81.18
	99.06	48.04	61.15	67.66		55.88	12.09	43.06	91.48
	101.60	46.23	58.48	70.14		63.50	14.57	58.66	85.57
	104.14	45.18	60.00	70.04		71.12	20.87	68.10	80.45
	109.22	43.42	55.72	66.89		78.74	32.44	65.63	76.12
	111.76	42.45	56.42	68.67		86.36	43.19	63.17	75.32
	114.30	41.76	55.78	68.30		93.98	44.59	60.70	72.74
	116.84	42.40	56.05	67.97		101.60	44.39	56.95	69.96
	119.38	41.72	54.72	67.57		109.22	43.05	56.26	69.20
	121.92	41.71	55.72	67.30		116.84	41.64	55.19	68.42
	124.46	41.07	55.41	67.68		124.46	39.97	54.15	66.28
	127.00	40.36	54.06	66.59		132.08	39.59	53.20	65.66
	129.54	38.31	52.66	65.34		139.70	36.62	52.23	65.23
	132.08	38.87	51.92	64.59		147.32	37.18	51.75	64.47
	134.62	37.52	51.55	64.56		162.56	35.67	48.60	62.74
	139.70	37.38	50.10	61.33		175.26	34.33	48.96	62.50
	144.78	38.45	51.46	63.39					

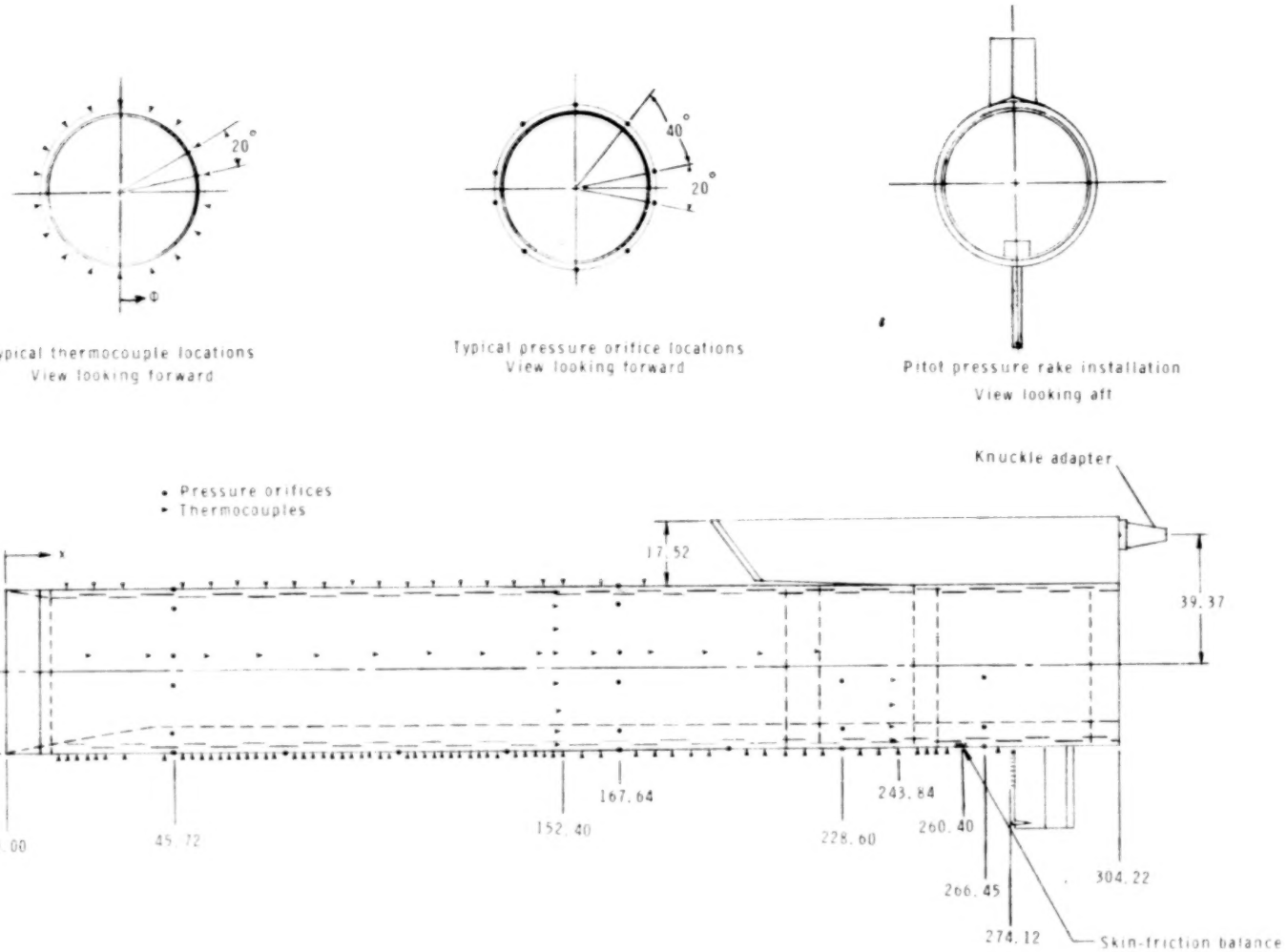

(a) Cylinder instrumentation.

Figure 1.- Location of instrumentation on hollow cylinder and boundary-layer pitot rake details.

Probe Number	y
1	0.312
2	0.506
3	0.693
4	0.887
5	1.057
6	1.435
7	2.098
8	2.703
9	3.312
10	3.934
11	4.547
12	5.159
13	6.440
14	7.645
15	8.940
16	10.215

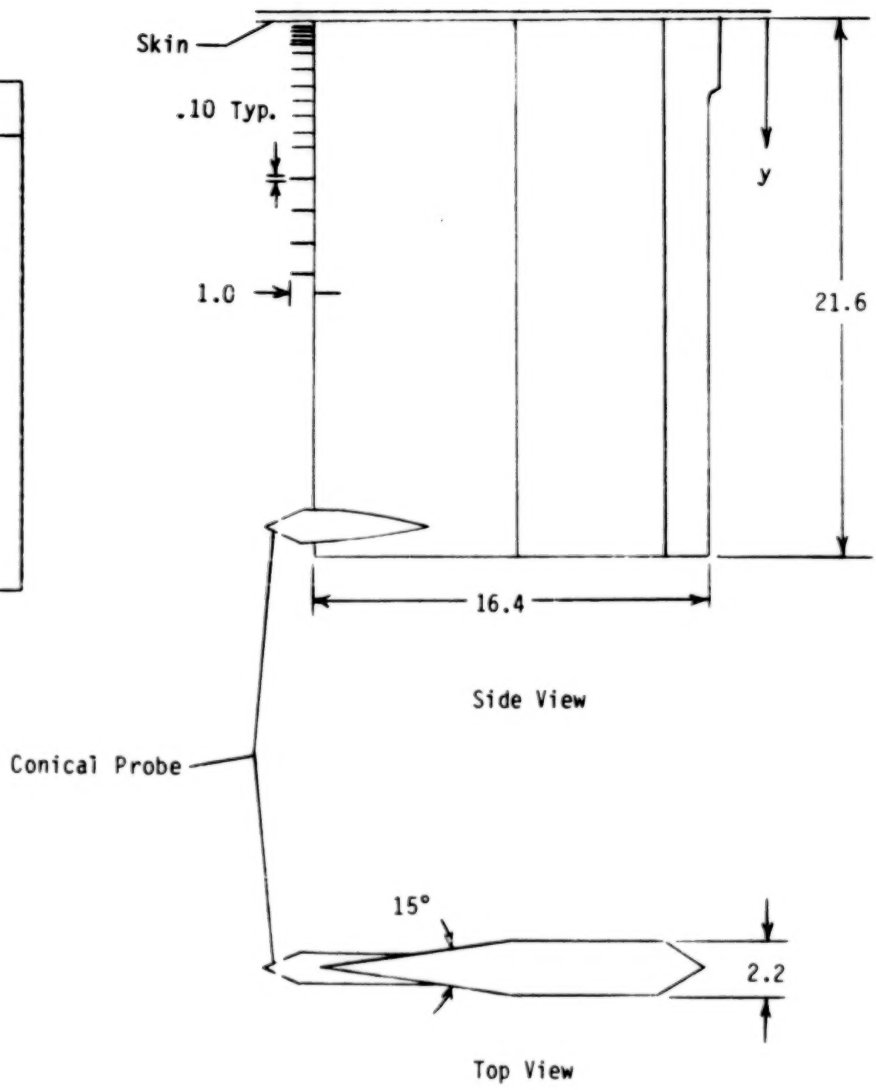

(b) Boundary-layer pitot pressure rake details.

Figure 1.- Concluded.

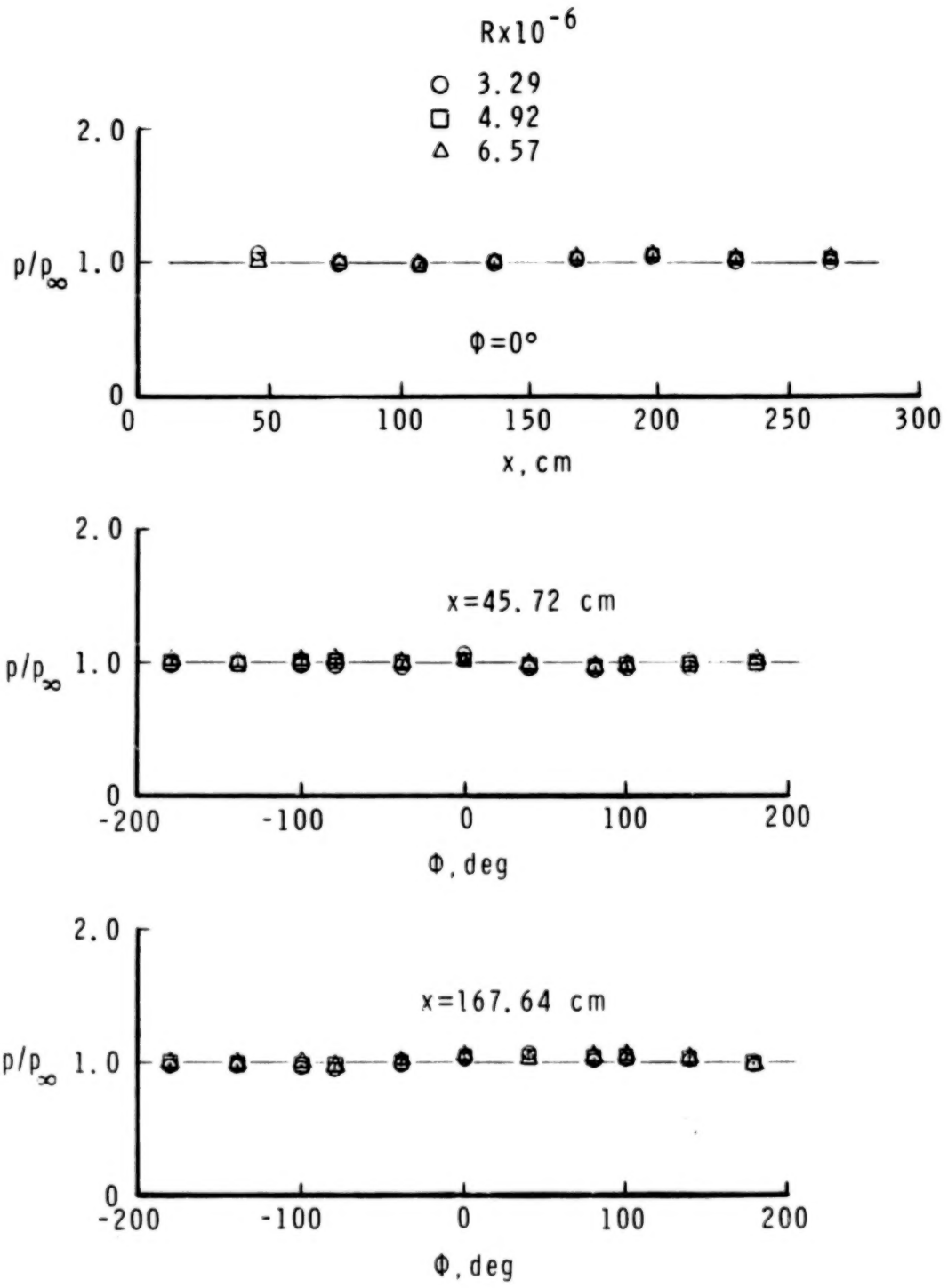

(a) Equilibrium wall temperature without transition grit.

Figure 2.- Typical longitudinal and circumferential pressure distribution.

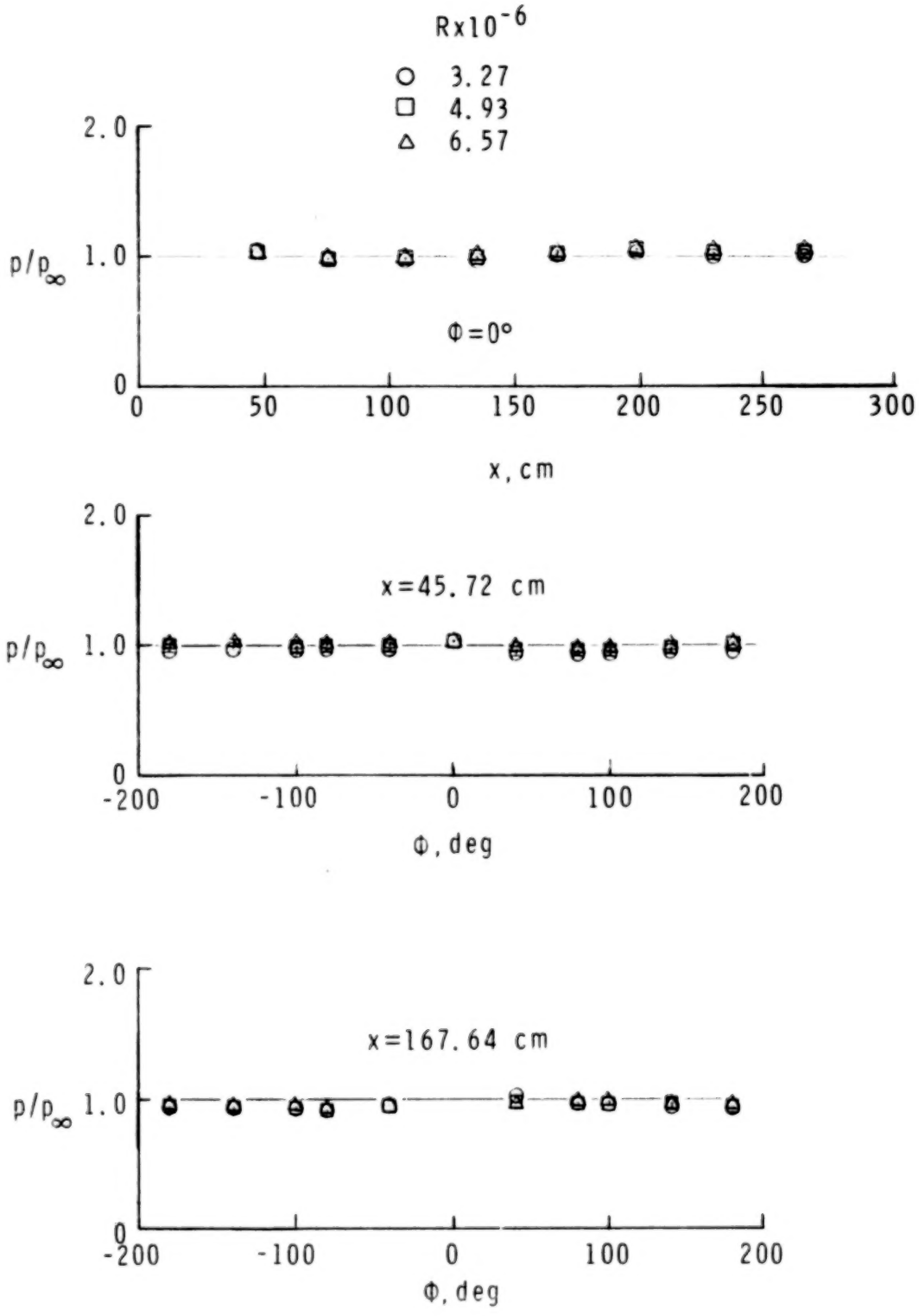

(b) Equilibrium wall temperature with No. 35 transition grit.

Figure 2.- Concluded.

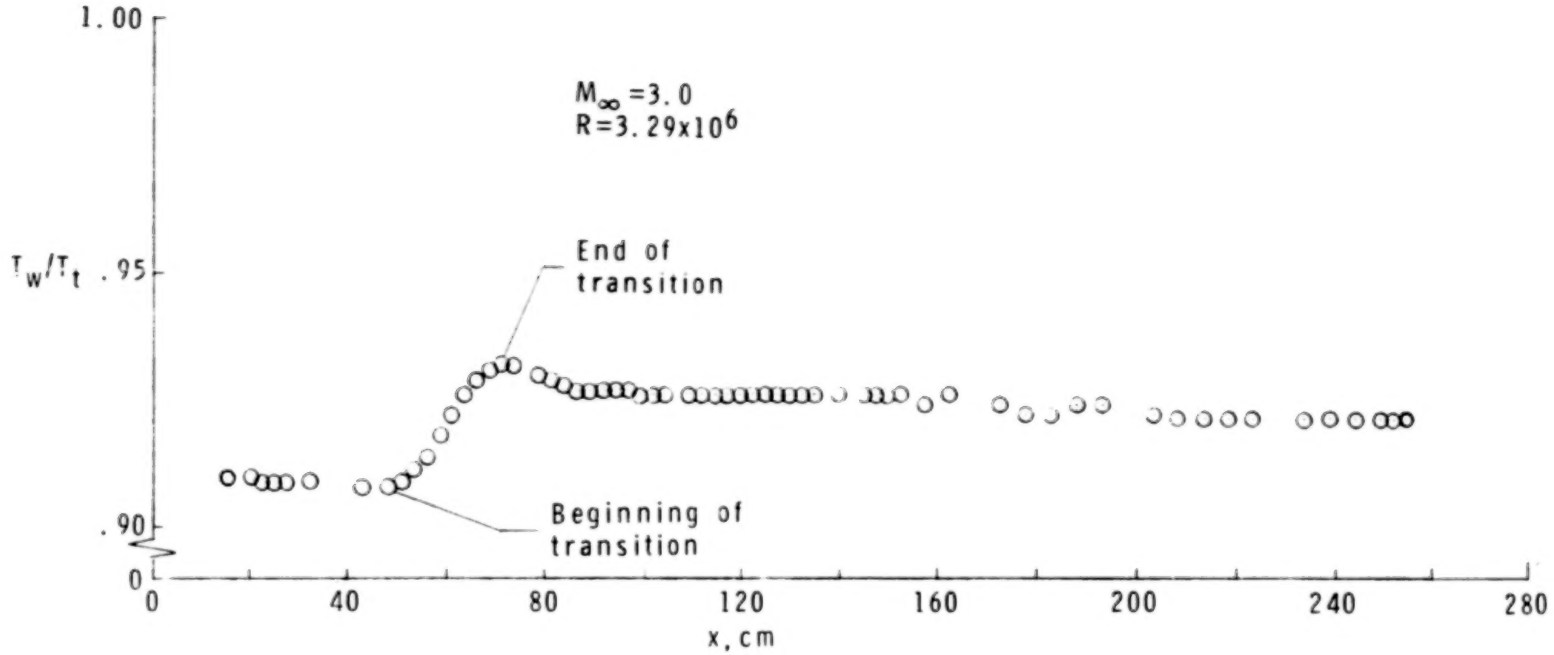

Figure 3.- Typical equilibrium wall temperature distribution. $\phi = 0^o$; without transition grit.

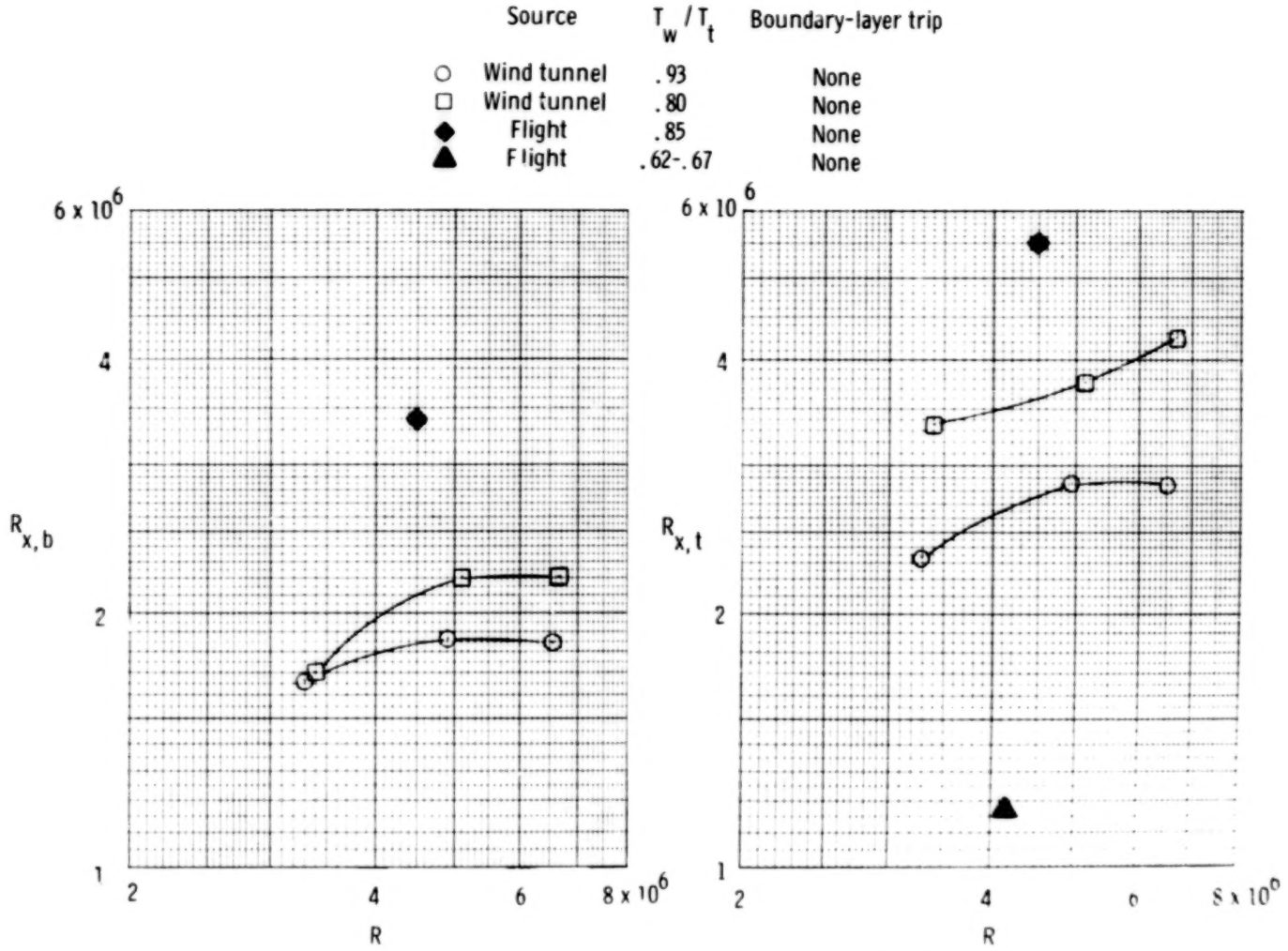

(a) Beginning of transition.

(b) End of transition.

Figure 4.- Comparison of flight and wind-tunnel transitional Reynolds numbers. M ≈ 3.

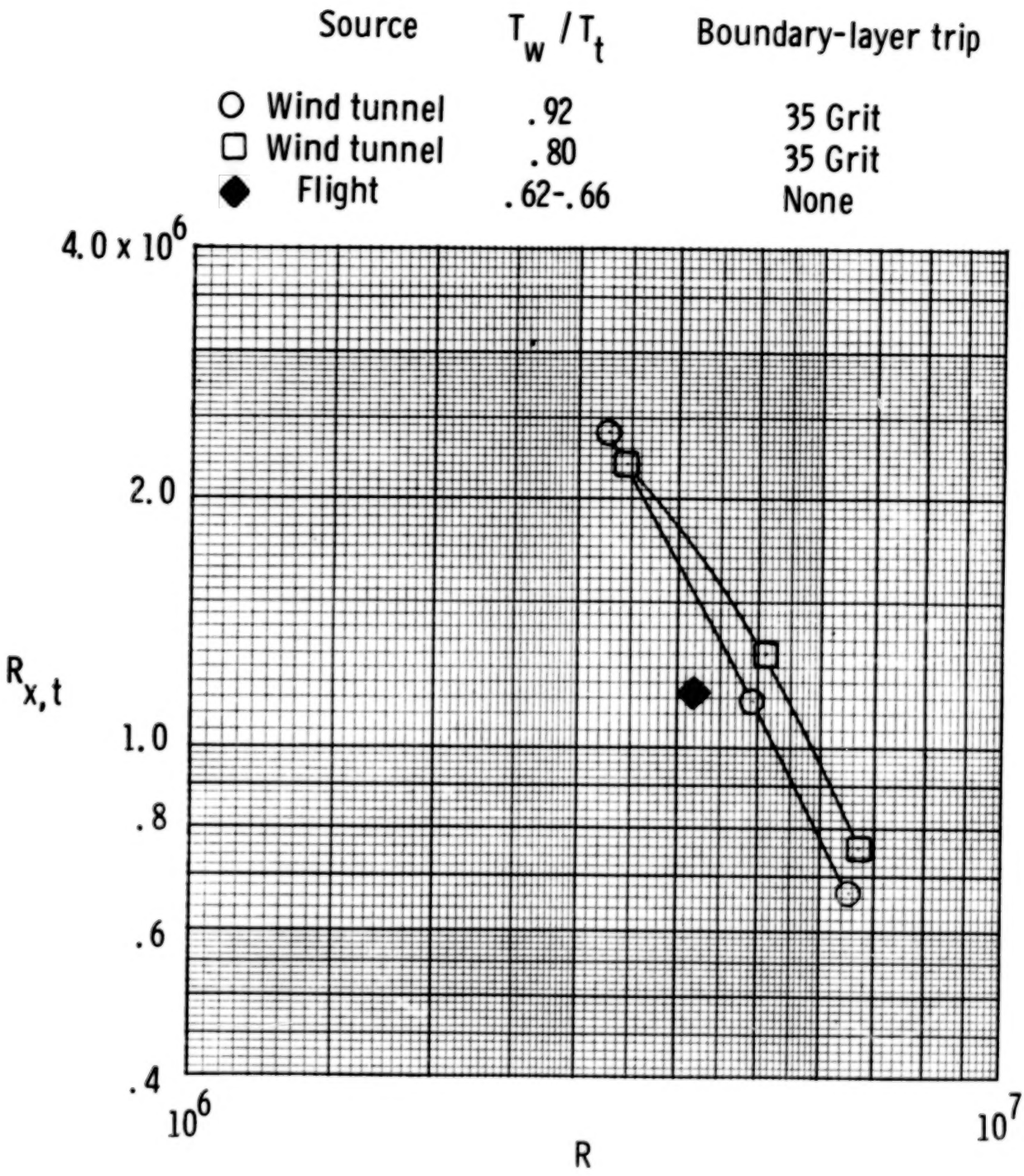

(c) End of transition.

Figure 4.- Concluded.

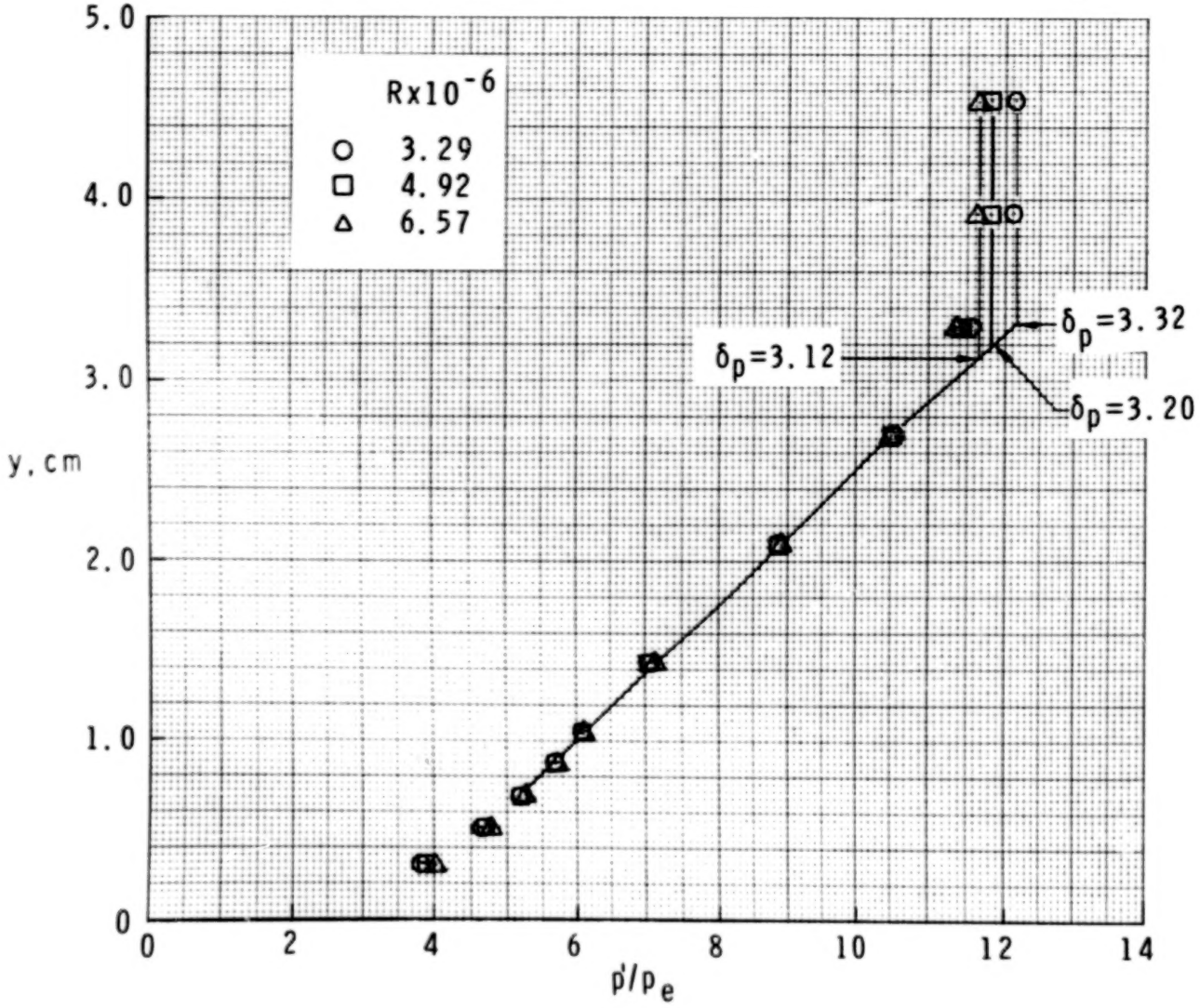

(a) Without transition grit.

Figure 5.- Determination of boundary-layer thickness from impact pressure measurements.

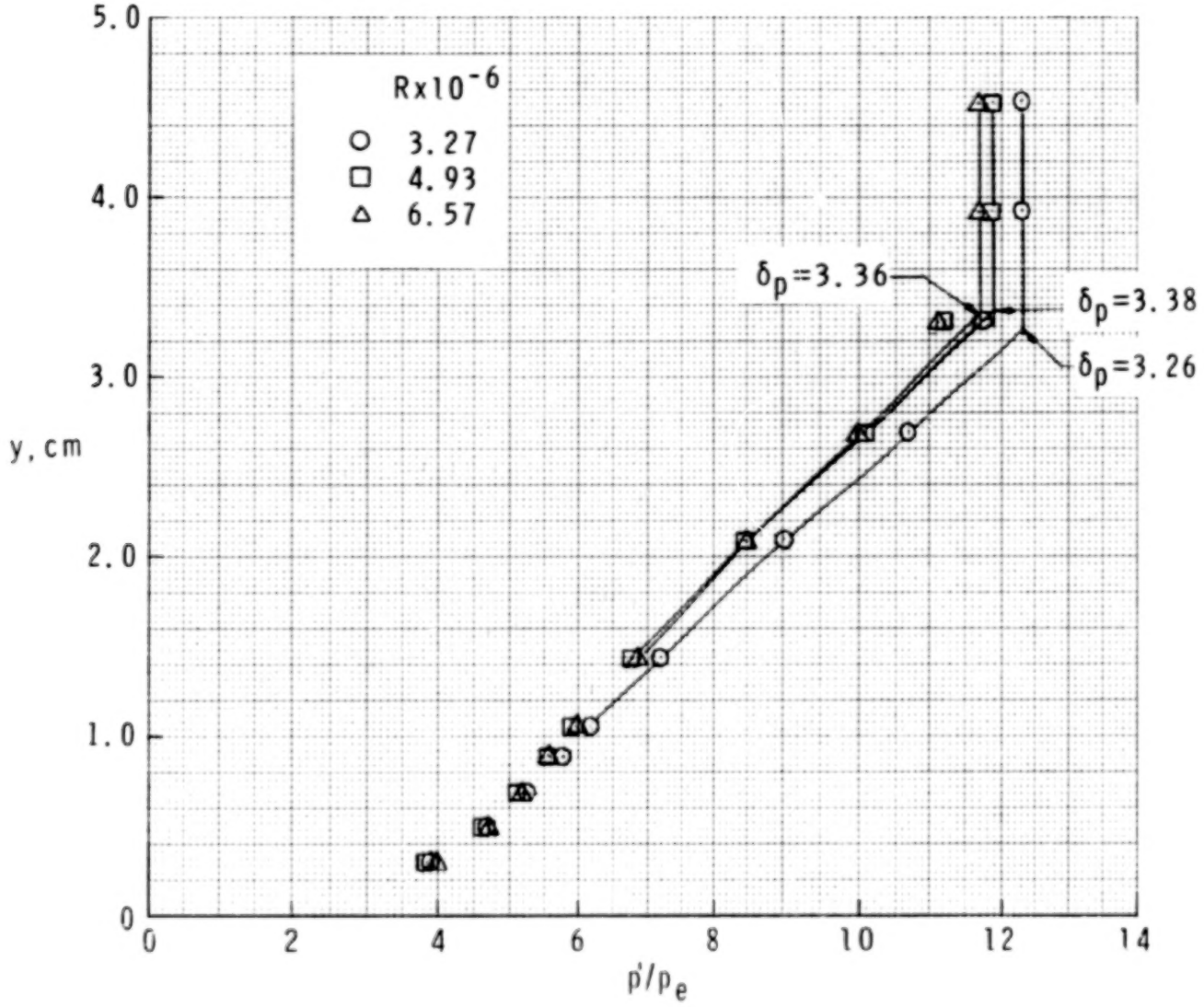

(b) No. 35 transition grit.

Figure 5.- Concluded.

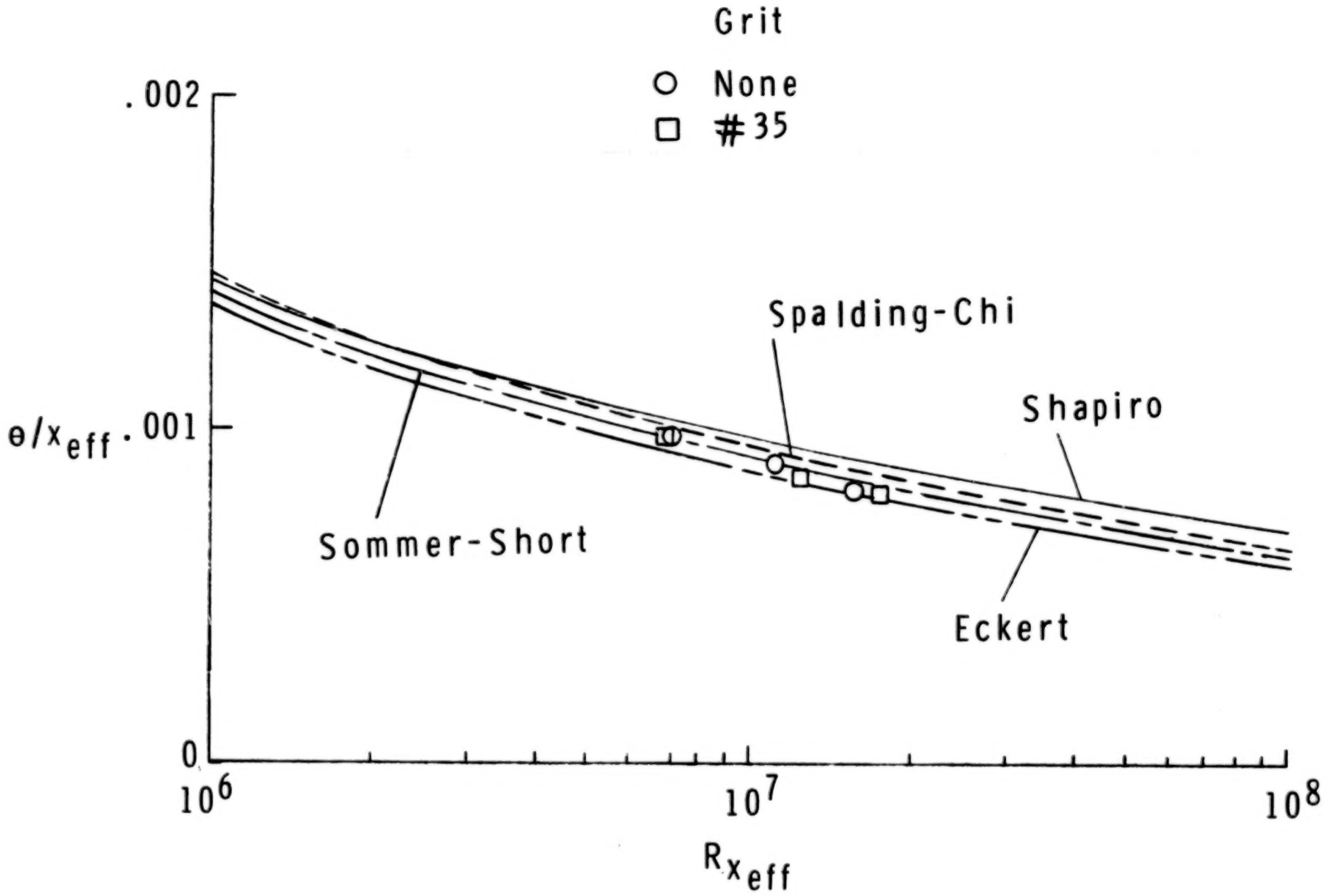

Figure 6.- Comparison of measured and calculated momentum thickness.

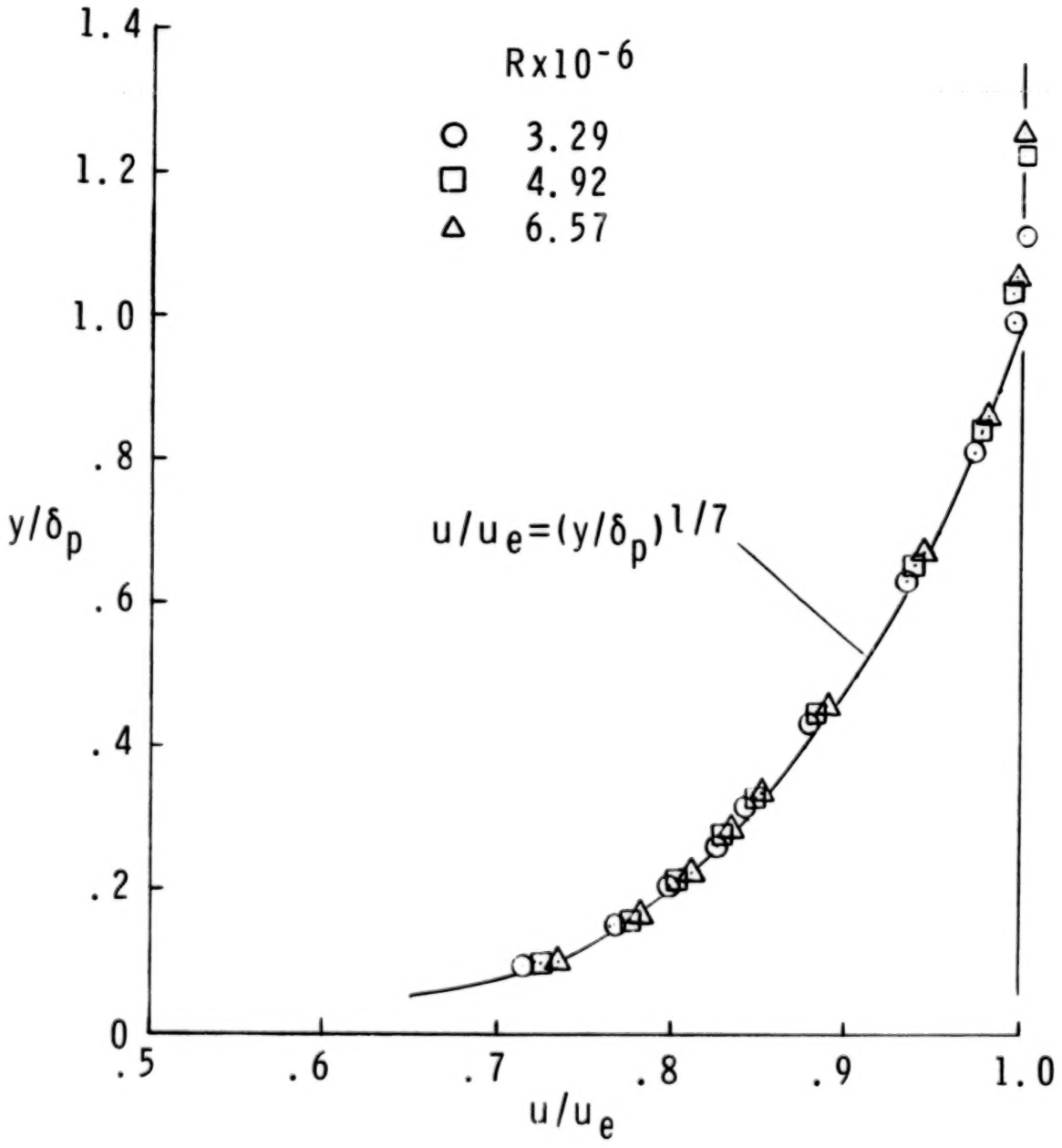

(a) Without transition grit.

Figure 7.- Comparison of measured nondimensional velocity profiles with power law relationship.

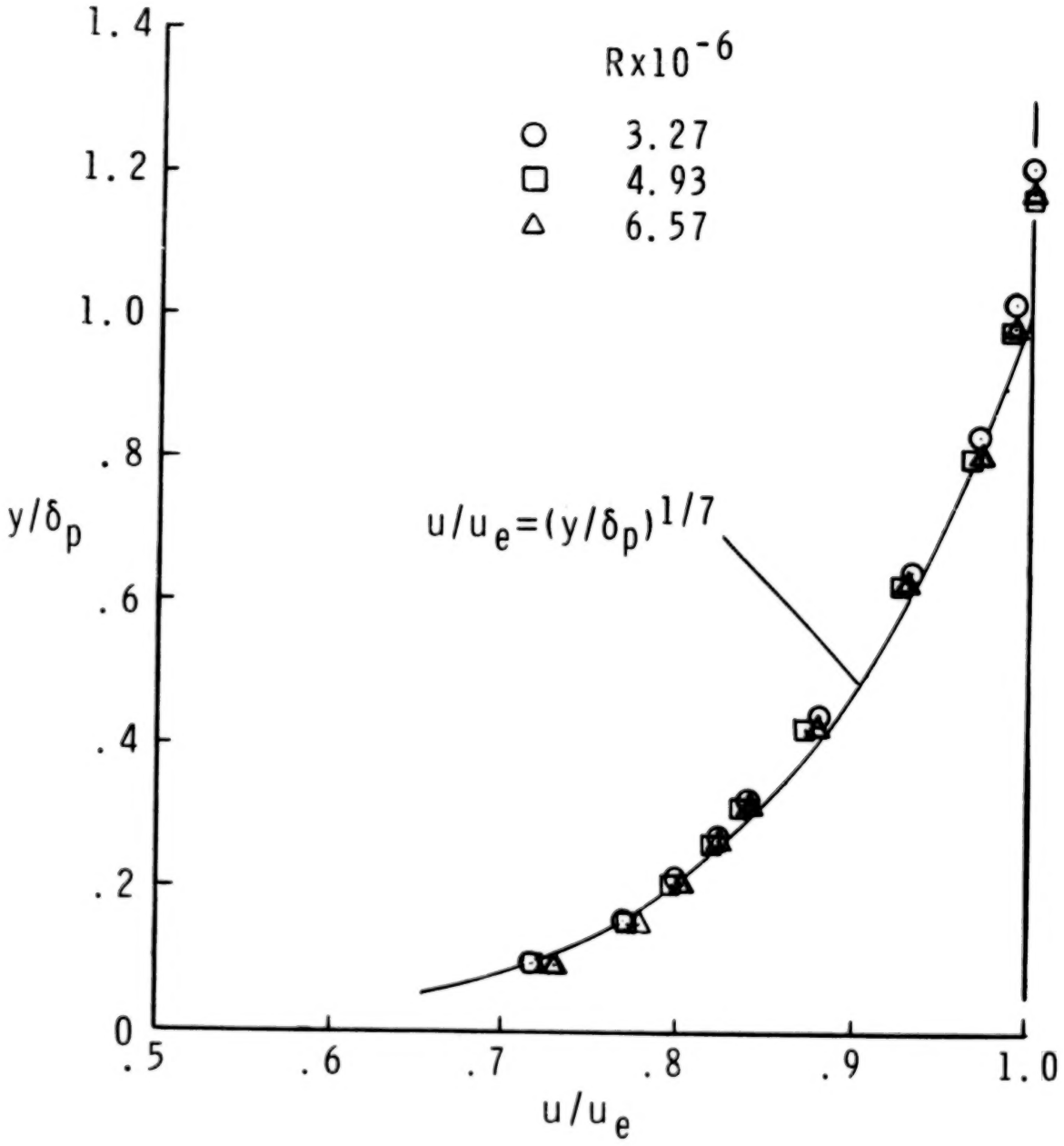

(b) No. 35 transition grit.

Figure 7.- Concluded.

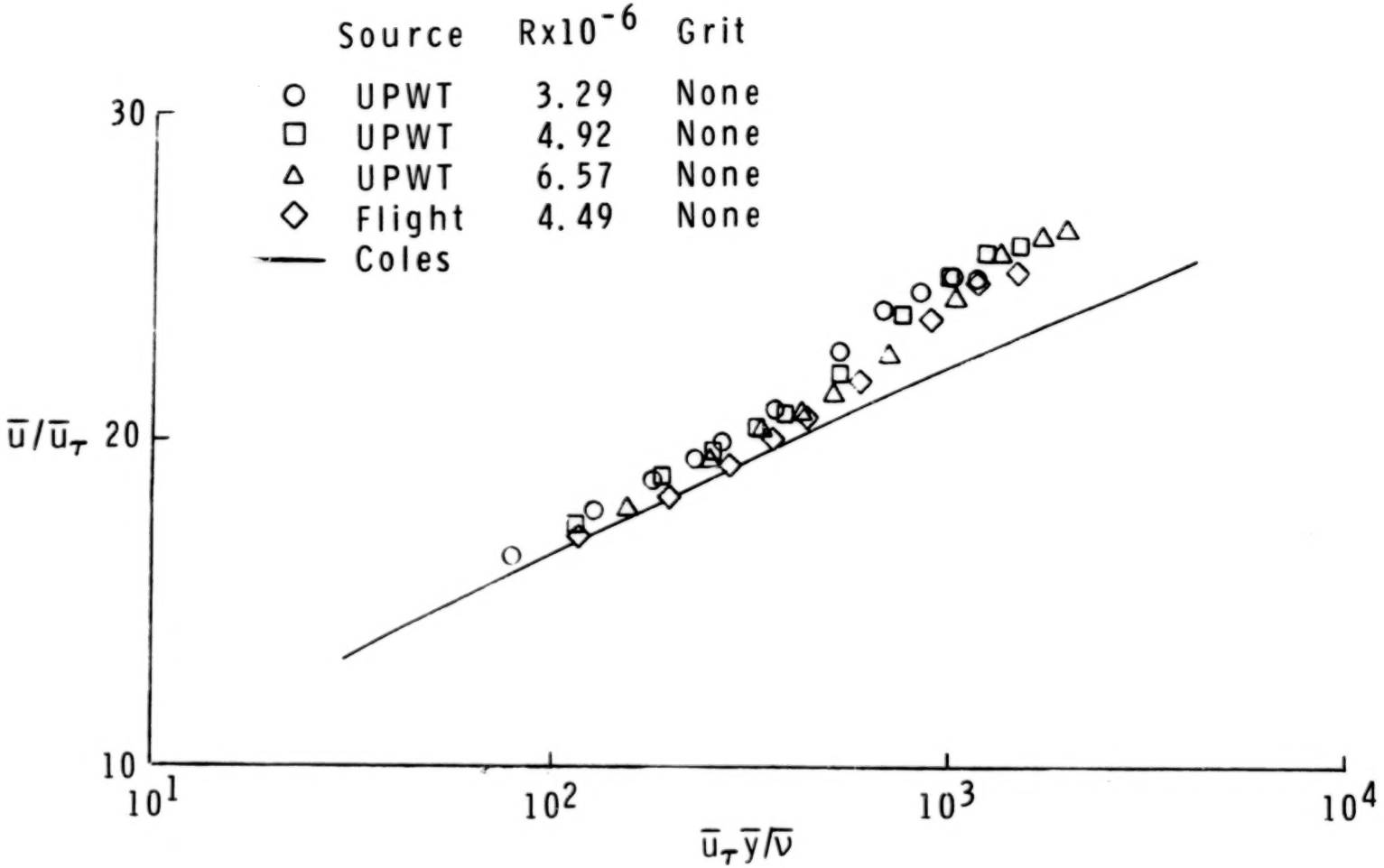

(a) Van Driest.

Figure 8.- Comparison of wind-tunnel, flight, and theoretical incompressible law-of-the-wall velocity profiles using several transformation theories.

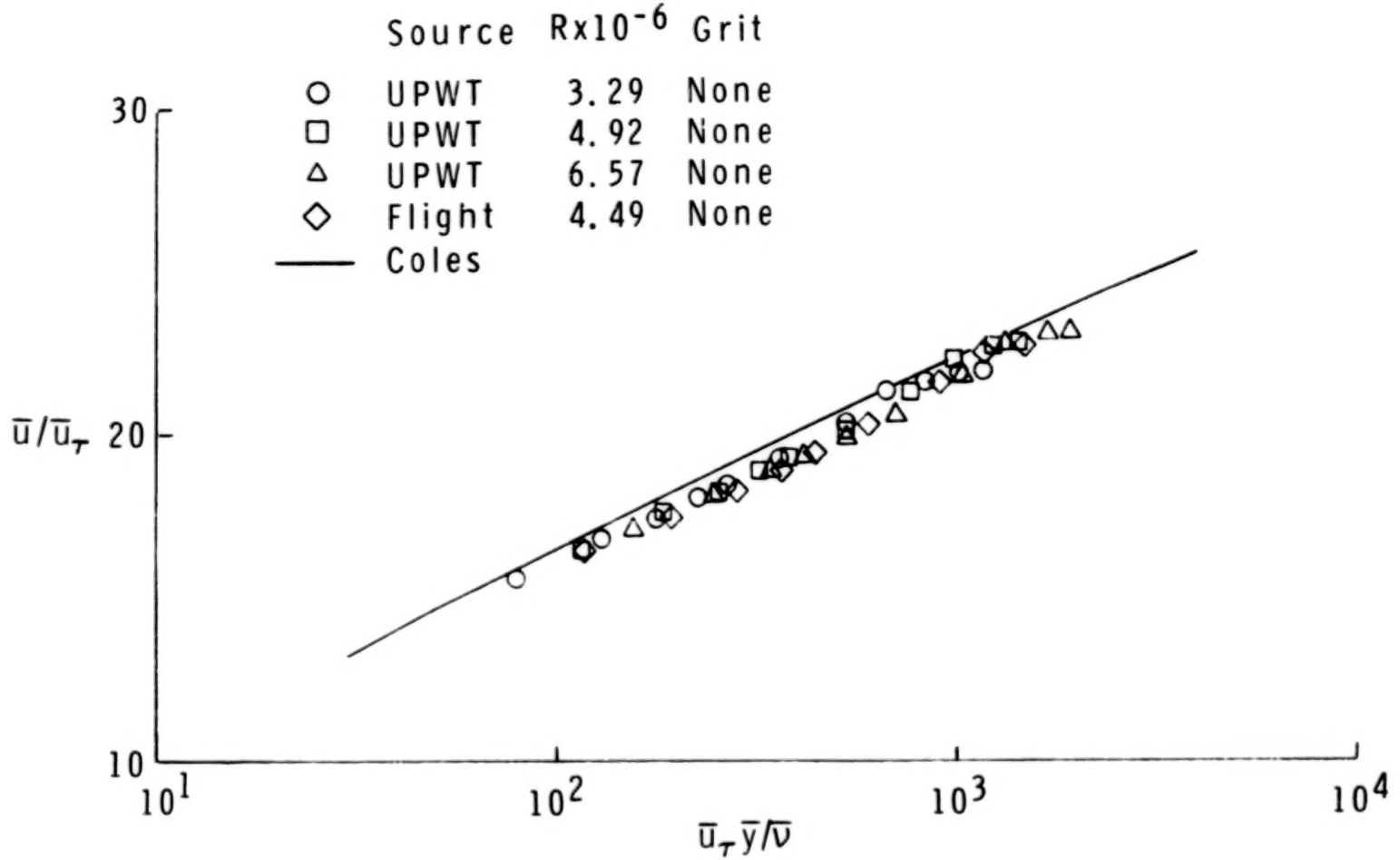

(b) Reference wall temperature.

Figure 8.- Continued.

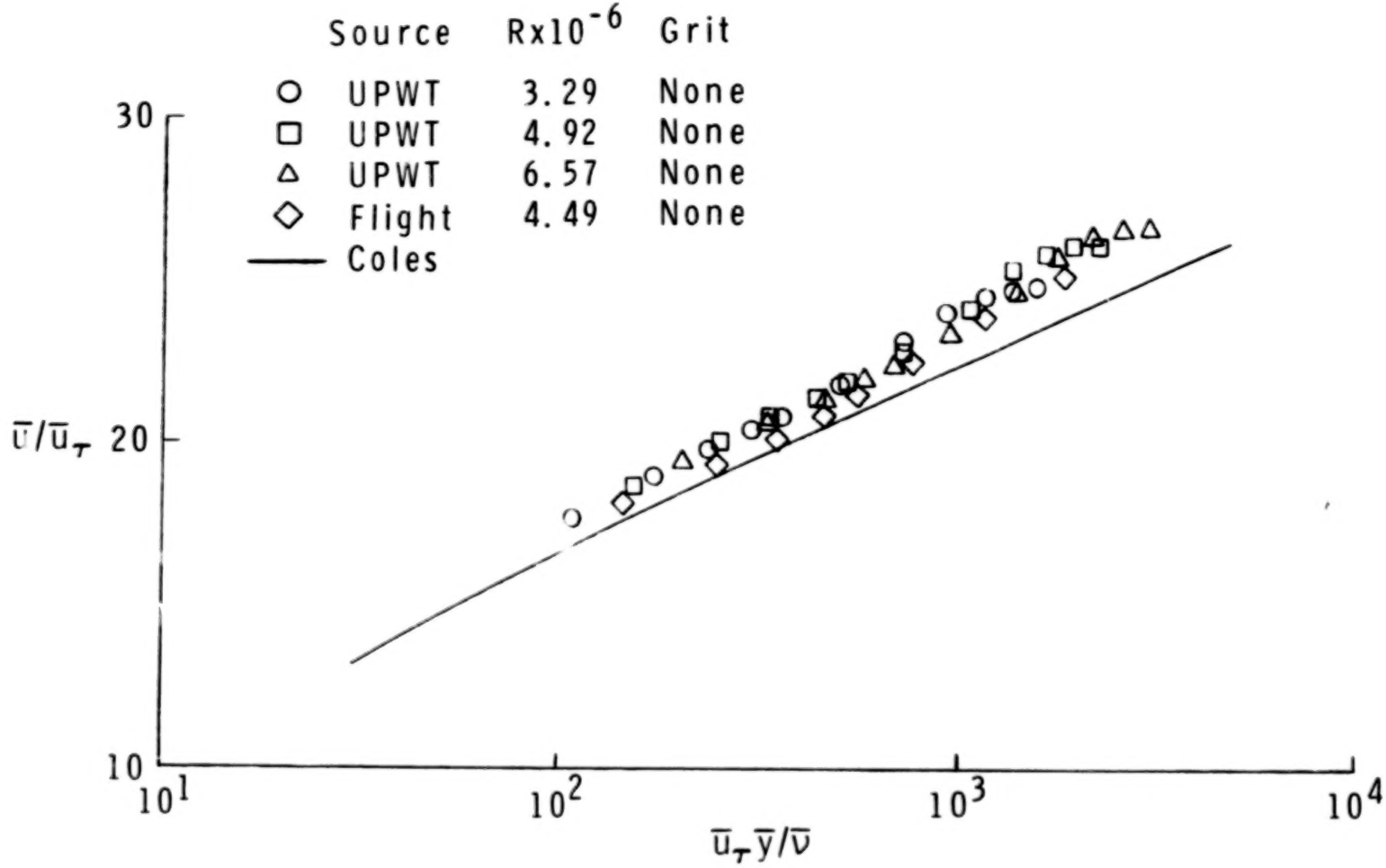

(c) Sommer and Short.

Figure 8.- Continued.

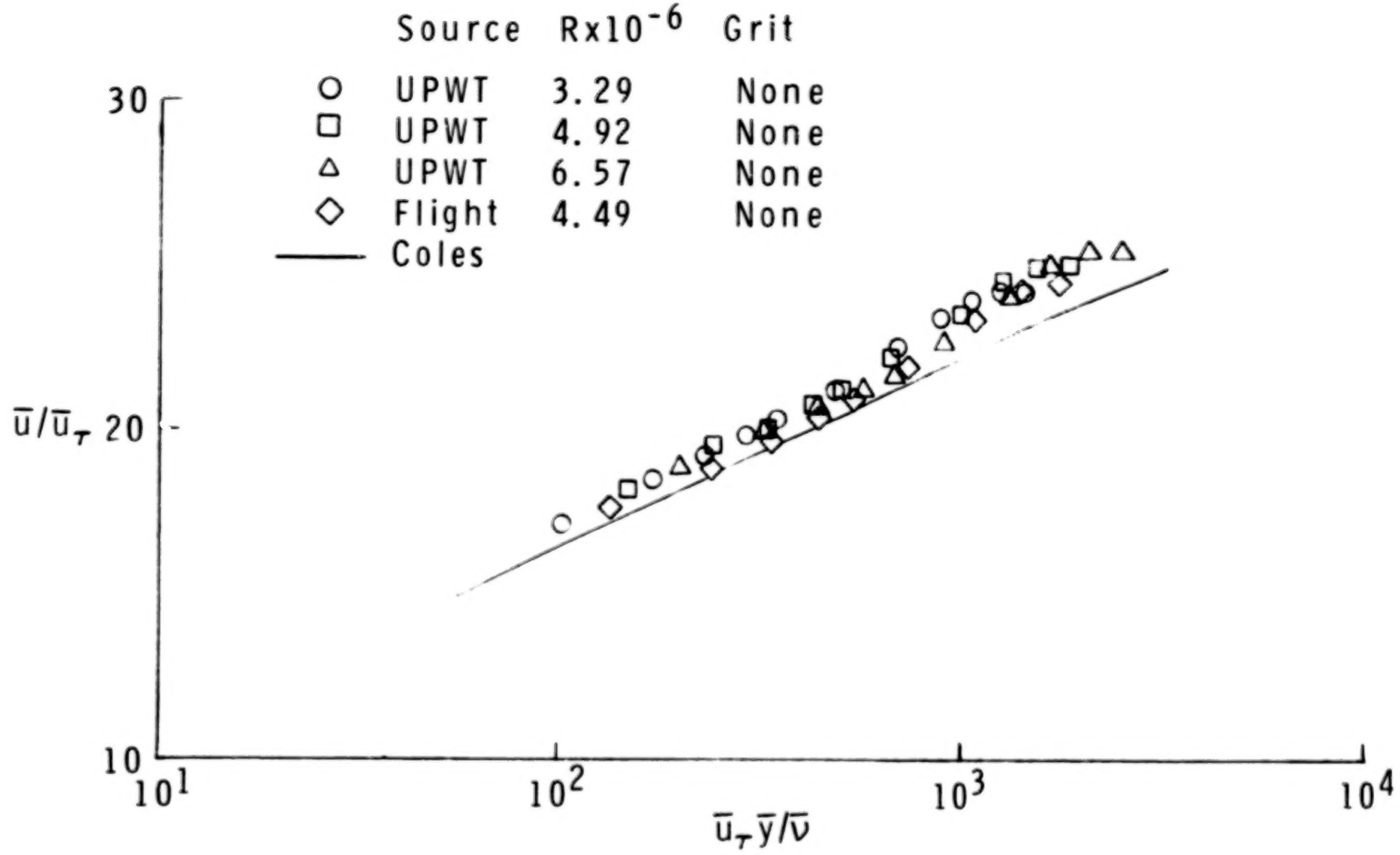

(d) Eckert reference temperature.

Figure 8.- Concluded.

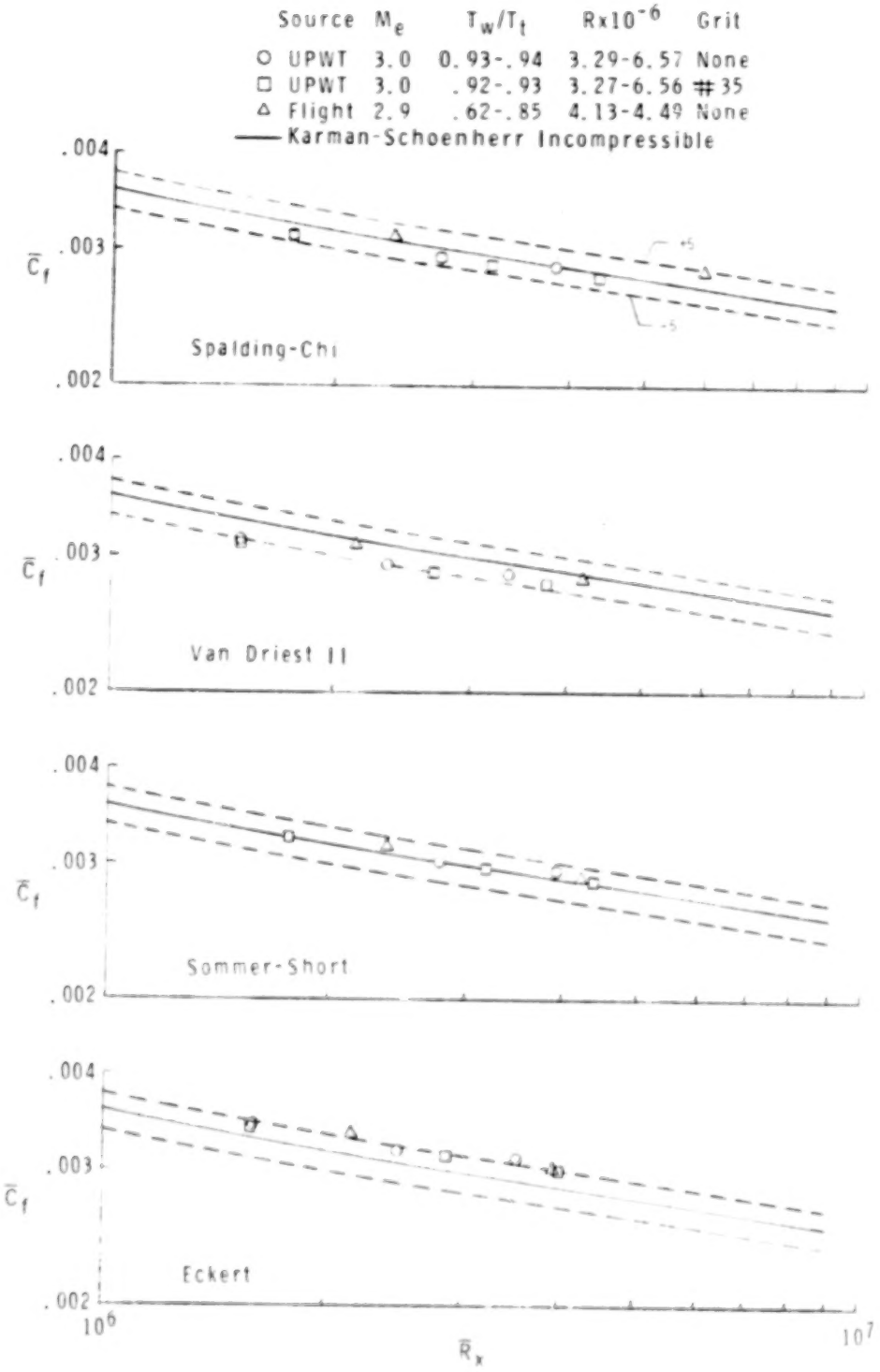

Figure 9.- Comparison of flight and wind-tunnel skin-friction data reduced by several methods.

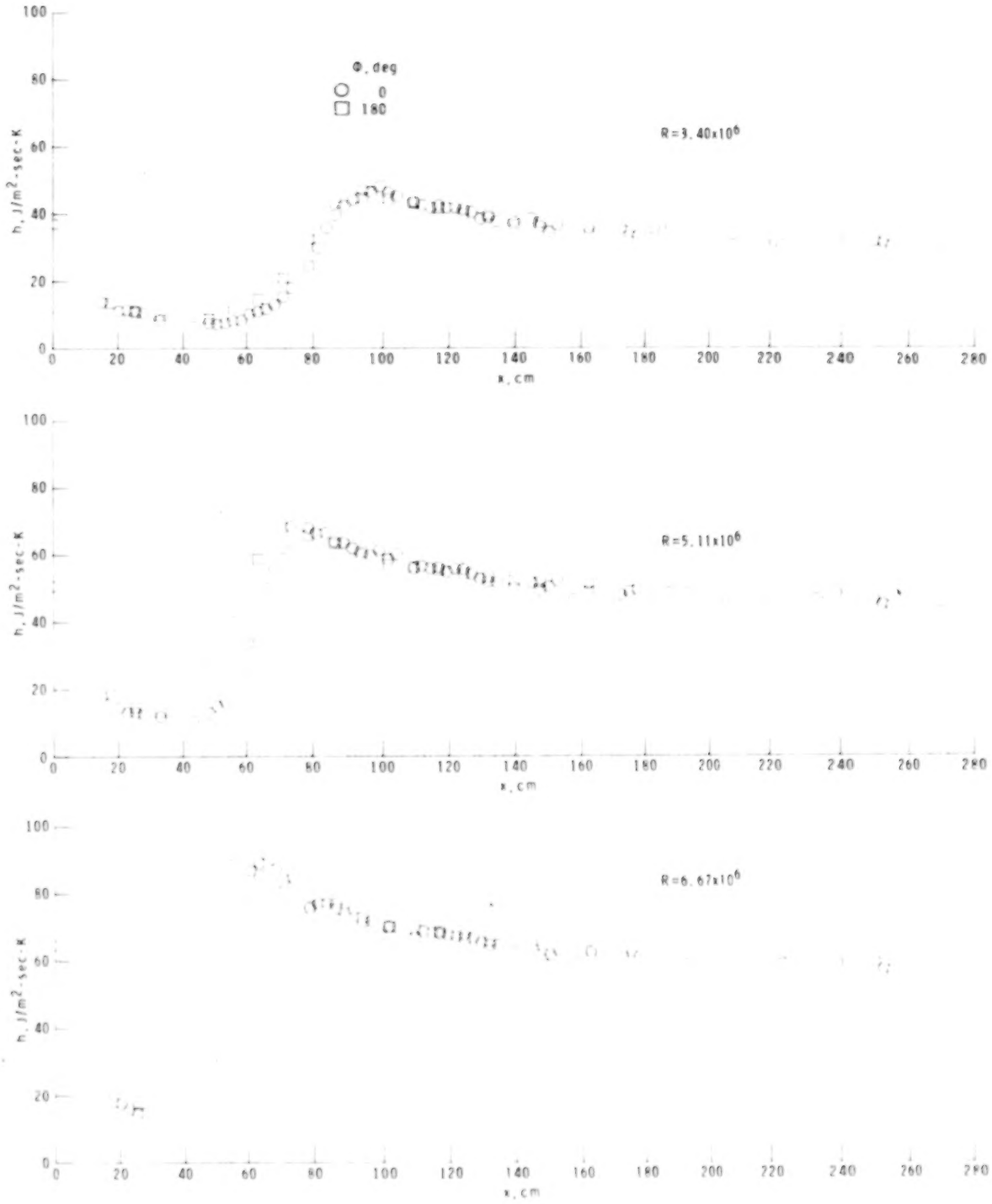

(a) Without transition grit.

Figure 10.- Typical wind-tunnel measured heat-transfer distribution.

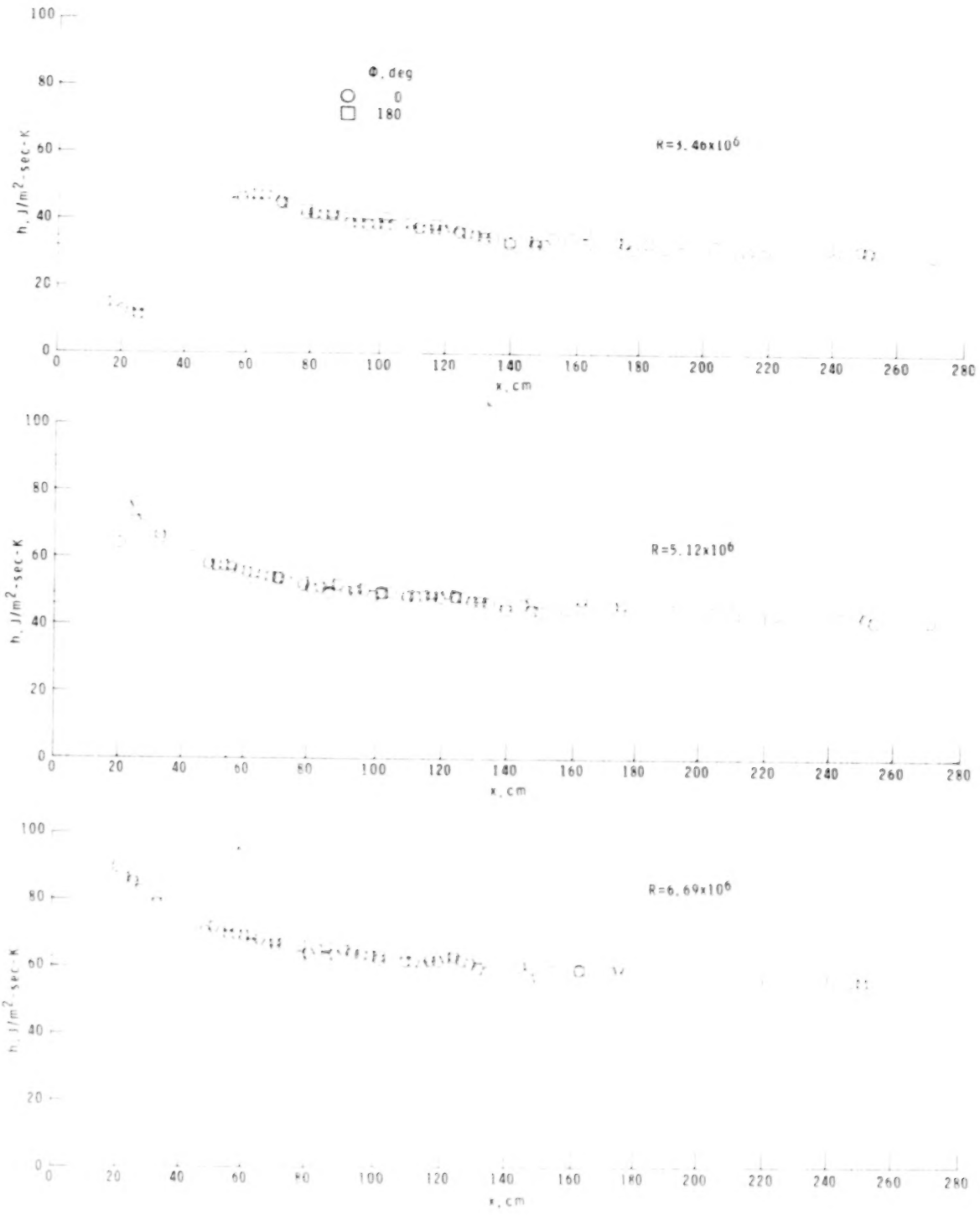

(b) No. 35 transition grit.

Figure 10.- Concluded.

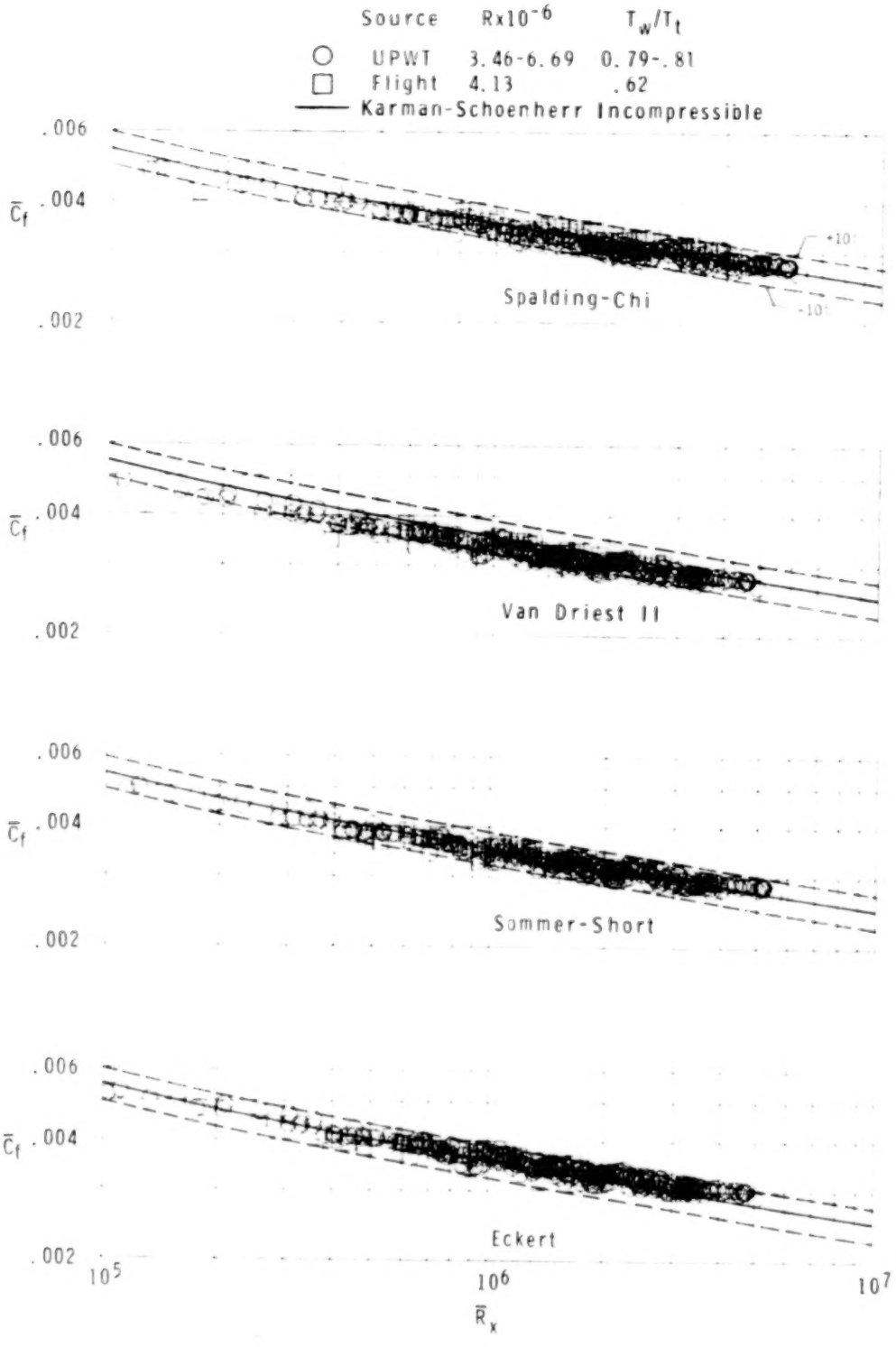

(a) Without transition grit.

Figure 11.- Comparison of flight and wind-tunnel heat-transfer measurements reduced by several methods.

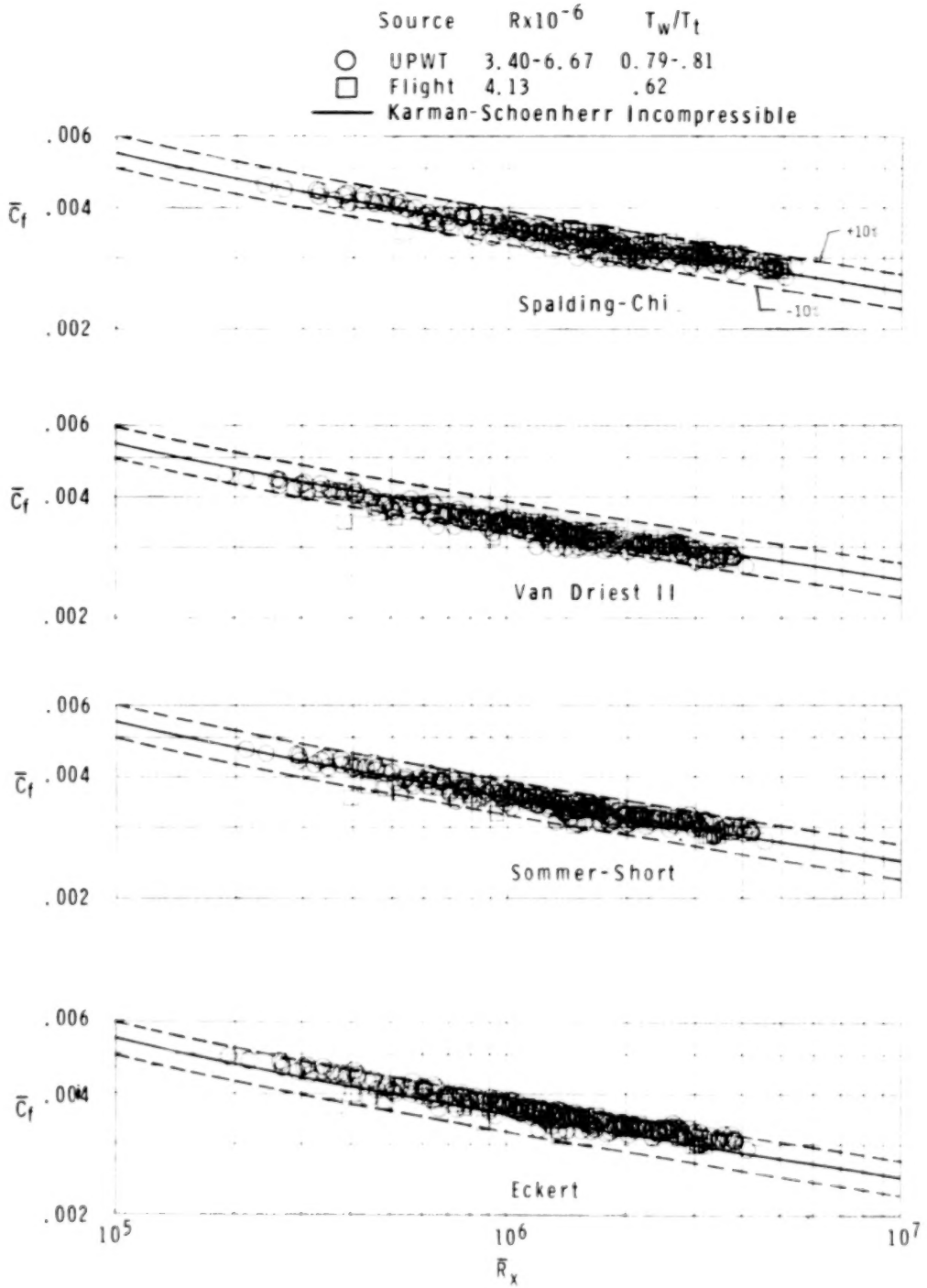

(b) No. 35 transition grit.

Figure 11.- Concluded.

1. Report No.	2. Government Accession No.	3. Recipient's Catalog No.
NASA TP-1789		

4. Title and Subtitle	5. Report Date
WIND-TUNNEL MEASUREMENTS AND COMPARISON WITH FLIGHT OF THE BOUNDARY LAYER AND HEAT TRANSFER ON A HOLLOW CYLINDER AT MACH 3	December 1980
	6. Performing Organization Code: 505-43-23-02
7. Author(s): Robert L. Stallings, Jr., and Milton Lamb	8. Performing Organization Report No.: L-14044
9. Performing Organization Name and Address: NASA Langley Research Center, Hampton, VA 23665	10. Work Unit No.
	11. Contract or Grant No.
12. Sponsoring Agency Name and Address: National Aeronautics and Space Administration, Washington, DC 20546	13. Type of Report and Period Covered: Technical Paper
	14. Sponsoring Agency Code

15. Supplementary Notes

16. Abstract

Wind-tunnel tests have been conducted to obtain boundary-layer and heat-transfer measurements on a hollow cylinder 304.22 cm in length and 43.70 cm in diameter for comparison with similar measurements that previously were obtained in flight with the same cylinder attached to the YF-12 airplane. The wind-tunnel tests were conducted both with and without boundary-layer trips at Mach 3 and nominal free-stream Reynolds numbers per meter ranging from 3.3×10^6 to 6.6×10^6. Instrumentation consisted of pressure orifices, thermocouples, a boundary-layer pitot pressure rake, and a floating element skin-friction balance. Measurements from both wind tunnel and flight are compared with existing engineering prediction methods.

17. Key Words (Suggested by Author(s))	18. Distribution Statement
Wind-tunnel measurements Flight measurements Supersonic Heat transfer Skin friction Boundary layer	Unclassified - Unlimited Subject Category 02

19. Security Classif. (of this report)	20. Security Classif. (of this page)	21. No. of Pages	22. Price
Unclassified	Unclassified	45	A03

For sale by the National Technical Information Service, Springfield, Virginia 22161

NASA-Langley, 1980

END

February 27, 1981